Summer 2016

Constrained-Energy Cross-Well Actuation of Bistable Structures

Masoud Zarepoor
Old Dominion University

CONSTRAINED-ENERGY CROSS-WELL ACTUATION OF BISTABLE STRUCTURES

by

Masoud Zarepoor
B.S. September 2010, Shiraz University, Iran
M.Sc. July 2013, Wright State University

A Dissertation Submitted to the Faculty of
Old Dominion University in Partial Fulfillment of the
Requirements for the Degree of

DOCTOR OF PHILOSOPHY

MECHANICAL ENGINEERING

OLD DOMINION UNIVERSITY
August 2016

Approved by:

Onur Bilgen (Director)

Sebastian Y Bawab (Member)

Mounir Laroussi (Member)

Dipankar Ghosh (Member)

ABSTRACT

CONSTRAINED-ENERGY CROSS-WELL ACTUATION OF BISTABLE STRUCTURES

Masoud Zarepoor
Old Dominion University, 2016
Director: Dr. Onur Bilgen

Bistable structures have two stable equilibrium positions and can be utilized to maintain a specific static shape with no energy consumption. This dissertation focuses on the minimum required energy for performing snap-through of a bistable structure. Snap-through is the motion of a bistable structure from one stable equilibrium position to the other. This research uses the Duffing-Holmes equation as a one-degree-of-freedom representative model of a bistable structure, and this nonlinear equation is solved to calculate the required energy for cross-well oscillation. The research identifies several unique features of the response of a bistable system subjected to force and energy constraints. The research also shows how the required energy for cross-well oscillation varies as a function of damping ratio, frequency ratio, and for different values of excitation force amplitudes. The response of the bistable system is compared to a mono-stable linear system with the same parameters. A magneto-elastic bistable beam was fabricated and tested to validate theoretical predictions.

This dissertation is dedicated my parents, Gholamhossein Zarepour and Sedigheh Golafshan, and to my best friend, Mohsen, who have always devoted themselves to make my dreams come true.

ACKNOWLEDGMENTS

First, I would like to thank my advisor, Dr. Onur Bilgen, for help and support. He has always been available for answering my questions and provided me all the required resources for conducting a successful research project.

Sincere thanks to my committee members, Dr. Sebastian Y. Bawab, Dr. Mounir Laroussi and Dr. Dipankar Ghosh for evaluating my research and giving me helpful feedback and suggestions.

I would like to acknowledge my colleagues in the Smart Systems Laboratory. I will never forget their support, motivation and kind behavior.

Thank you to my parents, Gholamhossein Zarepour and Sedigheh Golafshan, for supporting me while completing my education. I would not have been able to make progress without their guidance and self-sacrifice.

Thanks to the Department of Mechanical and Aerospace Engineering at Old Dominion University, especially to Dr. Sebastian Y. Bawab, for financial and logistical support.

This work was conducted in the Smart Systems Laboratory at Old Dominion University.

TABLE OF CONTENTS

Chapter Page

LIST OF TABLES

LIST OF FIGURES

Figure Page

Figure Page

Figure Page

Figure Page

Figure Page

Figure Page

CHAPTER 1

INTRODUCTION AND LITERATURE REVIEW

Bistability is defined as the capability of a structure to adopt two stable shapes and to be utilized to maintain a specific static shape with no energy consumption. This research investigates the minimum required energy for performing snap-through of a bistable structure. The motion of a bistable structure from one stable equilibrium position to the other is physically modeled as a jump phenomenon known as a snap-through. Snap-through behavior is exploited to convert small-scale displacements of actuators to large-scale ones. Figure 1-1 represents a bistable wing with piezoelectric actuators [1, 2].

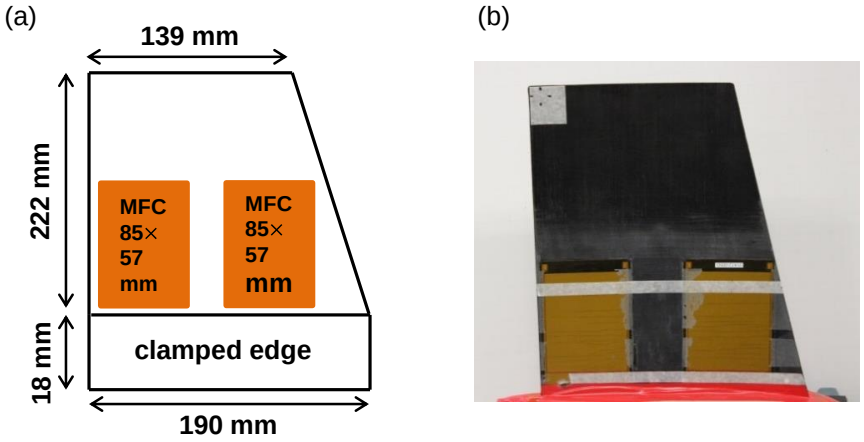

Figure 1-1. A cantilevered bistable wing with two surface-bonded piezoelectric actuators: (a) illustration (b) physical prototype [1, 2].

The following sections present the background related to this research. Section 1.1 provides a brief explanation of piezoelectric materials and demonstrates the most known structural theories on beams. Next, the bistability property, actuation of bistable

structures, and solution techniques are presented. Sections 1.2-1.4 provide the motivation, objectives, and the outline of the dissertation, respectively.

1.1. Background and Literature Review

The following sections present information on the piezoelectric materials, structural theories for beams, bistable structures, and solution techniques.

1.1.1. Piezoelectric Materials

Piezoelectric materials exhibit electromechanical coupling. They produce electrical charge when a mechanical stress is applied; this effect is known as the direct effect and has applications in sensing and harvesting vibrational energy. Piezoelectric materials deform by the application of an electric field, and this electrical-to-mechanical coupling is known as the converse piezoelectric effect. Converse piezoelectric effect is used for actuating different structures [3-5].

The properties of a piezoelectric material can be described by two mechanical variables and two electrical variables. Two mechanical variables are stress and strain, and two electric field variables are electric field and electric displacement. The direct and converse piezoelectric effects for a one-dimensional piezoelectric material can be described by two linear equations, which show the relationship between strain and electric displacement as a function of applied stress and applied electric field, shown in matrix form as follows:

$$\begin{bmatrix} S \\ D \end{bmatrix} = \begin{bmatrix} s & d \\ d & \varepsilon \end{bmatrix} \begin{bmatrix} T \\ E \end{bmatrix}. \tag{1-1}$$

In the above equation, S, D, T, and E are strain, electric displacement, applied stress, and applied electric field, respectively. Also, s, d, and ε are mechanical compliance, piezoelectric strain coefficient, and the dielectric permittivity, respectively.

The three-dimensional electromechanical behavior of a piezoelectric material is governed by the linear constitutive equations as follows [3]:

$$S_i = S_{ij}^E T_j + d_{ik} E_k \tag{1-2}$$

$$D_m = d_{mj} T_j + \varepsilon_{mk}^T E_n. \tag{1-3}$$

The superscript E shows constant electric field, and the superscript T indicates constant stress. The matrix form of the constitutive equations is [5]:

$$\begin{bmatrix} S_1 \\ S_2 \\ S_3 \\ S_4 \\ S_5 \\ S_6 \end{bmatrix} = \begin{bmatrix} S_{11}S_{12}S_{13}S_{14}S_{15}S_{16} \\ S_{21}S_{22}S_{23}S_{24}S_{25}S_{26} \\ S_{31}S_{32}S_{33}S_{34}S_{35}S_{36} \\ S_{41}S_{42}S_{43}S_{44}S_{45}S_{46} \\ S_{51}S_{52}S_{53}S_{54}S_{55}S_{56} \\ S_{61}S_{62}S_{63}S_{64}S_{65}S_{66} \end{bmatrix} \begin{bmatrix} T_1 \\ T_2 \\ T_3 \\ T_4 \\ T_5 \\ T_6 \end{bmatrix} + \begin{bmatrix} d_{11}d_{12}d_{13} \\ d_{21}d_{22}d_{23} \\ d_{31}d_{32}d_{33} \\ d_{41}d_{42}d_{43} \\ d_{51}d_{52}d_{53} \\ d_{61}d_{62}d_{63} \end{bmatrix} \begin{bmatrix} E_1 \\ E_2 \\ E_3 \end{bmatrix} \tag{1-4}$$

$$\begin{bmatrix} D_1 \\ D_2 \\ D_3 \end{bmatrix} = \begin{bmatrix} d_{11}d_{12}d_{13}d_{14}d_{15}d_{16} \\ d_{21}d_{22}d_{23}d_{24}d_{25}d_{26} \\ d_{31}d_{32}d_{33}d_{34}d_{35}d_{36} \end{bmatrix} + \begin{bmatrix} \varepsilon_{11}\varepsilon_{12}\varepsilon_{13} \\ \varepsilon_{21}\varepsilon_{22}\varepsilon_{23} \\ \varepsilon_{31}\varepsilon_{32}\varepsilon_{33} \end{bmatrix} \begin{bmatrix} E_1 \\ E_2 \\ E_3 \end{bmatrix}. \tag{1-5}$$

1.1.2. Structural Modeling of Beams

Several beam theories exist for modeling a beam in response to an external force or a bending moment. These theories are different in the mathematical description of strain through the beam thickness. The most well-known beam theories are: the Euler-Bernoulli beam theory, the Rayleigh beam theory, and the Timoshenko beam theory.

The Euler-Bernoulli beam theory assumes that the cross sectional area of a beam is rigid and does not distort with the application of a bending moment. Also, it is assumed that the cross sectional area remains perpendicular to the neutral axis after deflection of the beam. This theory is mainly utilized for slender beams with high length-to-thickness ratio. As a result, the effects of shear distortion and rotary inertia

can be neglected. The Euler-Bernoulli equation for the transverse vibration of a beam is [6]:

$$\rho A \frac{\partial^2 w(x,t)}{\partial t^2} + YI \frac{\partial^4 w(x,t)}{\partial x^4} = q(x,t). \quad (1\text{-}6)$$

In the above equation, ρ is the beam density, A is the cross-sectional area, $w(x,t)$ is the beam transverse deflection, I is the beam area moment of inertia, and q is the applied load per unit length.

The Rayleigh beam theory improves the Euler-Bernoulli beam model by adding the effect of rotary inertia; this effect is included by adding a term to the inertial component in Euler-Bernoulli beam equation. The Rayleigh beam theory equation for the transverse motion of a beam is:

$$\rho A \frac{\partial^2 w(x,t)}{\partial t^2} + YI \frac{\partial^4 w(x,t)}{\partial x^4} - \rho I \frac{\partial^4 w(x,t)}{\partial t^2 \partial x^2} = q(x,t). \quad (1\text{-}7)$$

The Timoshenko beam theory considers both the effect of rotary inertia and the effect of shear deformation. The Timoshenko beam theory is used to model the dynamics of beams with moderate length-to-thickness ratios. In the Timoshenko beam theory, the cross-sectional area of a beam distorts and does not remain perpendicular to the neutral axis with the application of a bending moment, due to the consideration of the effect of shear deformation [6, 7].

Figure 1-2 represents the predicted deflected cross-sectional areas of a beam by the Euler-Bernoulli and the Timoshenko beam theories. As can be seen in the figure, the cross-sectional area distorts for the Timoshenko beam theory, and it does not remain perpendicular to the neutral axis after deflection.

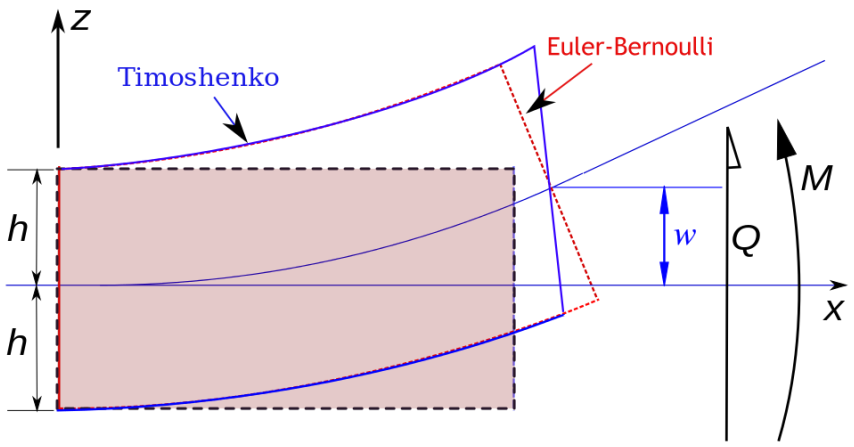

Figure 1-2. Deflected cross-sectional areas of a beam predicted by Euler-Bernoulli and Timoshenko beam theories [8].

1.1.3. Bistable Structures

Bistable structures are able to adopt two stable shapes and have applications in different areas, including common electronic devices such as switches [9-11], relays [12, 13], memory cells [14], control surfaces for morphing aircraft [2, 15-17], and in wind turbine blades for load alleviation [18]. The bistability property can be achieved in buckled beams and plates such as in cross-ply composite plates due to residual thermal stresses induced during the curing process [1, 19-23], slender beams under an axial compressive force [24-26], or beams buckled between two magnets [27]. The motion from one stable state to another is physically modeled as a jump phenomenon known as snap-through, and is exploited in actuators designed to produce large displacements with a small amount of actuation energy [15, 20, 28-30].

Bistability can be achieved in beams by applying an axial compressive force to them; the compressive force induces buckling in a beam. Several approaches exist to generate an axial compressive force. Figure 1-3 represents a cantilevered beam, buckled under an axial compressive force. As observed in the figure, the beam is bistable and can stand at the position of either A or B.

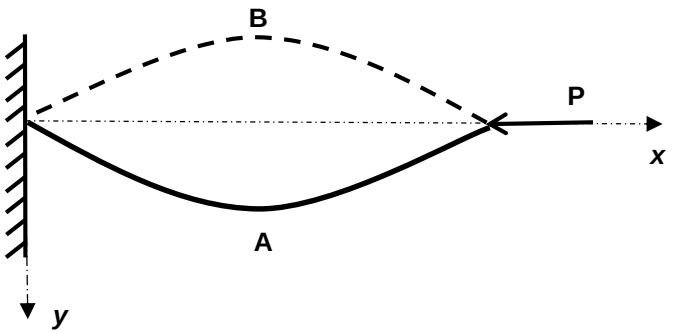

Figure 1-3. A buckled beam under an axial compressive force with two stable positions of A and B.

Lindberg et al. [24] demonstrated the buckling behavior of a beam due to an axial compressive force generated by temperature rise. The beam was subjected to a generalized temperature. The beam shows a smooth transition into one of the stable equilibrium positions at the bifurcation load.

Fang and Wickert [25] studied the static deformation of a beam, in the prebuckling and postbuckling regions, applied to an axial compressive force generated by a residual stress. It was found that the fabricated beams show continuous growth of deflection, in contrast to sudden bifurcation, at a critical load by considering the effect of imperfections, such as fabrication defects or non-ideal loading.

Vangbo [26] proposed a theoretical method to model the snap-through of a beam subjected to a known axial compressive force and a transverse compressive force. The transverse force changes the snap-through path and can be tuned to set the magnitude of critical axial force, required for buckling.

Saif [29] fabricated a tunable bistable micro-electro-mechanical system (MEMS). The system consists of a long slender micromechanical beam, attached to an actuator. The actuator applies an axial compressive force to make the beam bistable. A closed-form relation between the actuation force and the location of stable equilibrium is presented in this paper.

Tseng and Dugundji [31] described the chaotic motion and the snap-through behavior of a bistable buckled beam analytically and experimentally. Holmes [32] further explored the behavior of a bistable buckled beam in a more detailed manner.

Moon and Holmes [27] presented a bistable beam buckled between two magnets. They developed a lumped-parameter model based on linear elastic and nonlinear magnetic forces.

Bistability can be achieved in cross-ply composite plates due to residual stress, as mentioned earlier. Residual stresses build up during the curing process of multi-layered composite plates with different fiber orientations. Hufenbach et al. [19] proposed a modified stability analysis to predict the multistable deformation states of a fiber-reinforced composite due to thermal effects, moisture absorption and chemical shrinkage. The proposed method is capable of precise assessment of the design parameters for the construction of novel adaptive structures.

1.1.4. Piezoelectric Actuation of Bistable Structures

Improving energy features of piezoelectric actuators has been an important area of research, and a number of models are proposed to predict the energy consumption of a piezoelectric actuator.

Sun and Tong [33] determined the optimal voltage to control the static shape of composite plates using nonlinear piezoelectric actuators.

Liang [34] presented a coupled electro-mechanical model of a piezoceramic actuator integrated in a one-degree-of-freedom mechanical system to predict the actuator energy consumption and energy transfer from the actuator to the mechanical system.

Brennan and McGowan [35] proposed a method to predict the power consumption of a piezoelectric actuator used for active vibration control. They found

that the required power is independent of the dynamics between the surface-bonded piezoelectric actuator and the controlled structure.

Sirohi and Chopra [36] demonstrated the design of a tuned inductor-capacitor (L-C) oscillator circuit for piezoelectric actuators. These actuators have high capacitance and need large electric currents to be driven. Large currents result in excessive heat generation. Using an L-C oscillator circuit reduces the required power for driving a piezoelectric actuator by decreasing the required electric current.

Several important papers, studying the power consumption of a piezoelectric actuator were presented previously. These papers present different methods for calculating the power consumption of a piezoelectric actuator and propose various approaches for reducing the required power. However, piezoelectric actuators have small deformation outputs and cannot be used directly for large shape changes. Nonlinear mechanisms are utilized to increase the stroke of piezoelectric actuators and transform micron-scale displacements of actuators into large, millimeter-scale ones. Specifically, buckling is an effective way to achieve large displacements using piezoelectric actuators.

Lesieutre et al. [37] demonstrated the effect of mechanical nonlinearity on the electromechanical transformation coefficient. The piezoelectric beam actuator showed an apparent coupling coefficient of 1, which corresponds to perfect electromechanical conversion, for the axial compressive load equal to the buckling load.

Maurini et al. [30] proposed the multi-parameter actuation of a bistable beam and investigated different transition paths between two stable equilibria in terms of stability properties and energetic requirements. Three voltages are utilized for performing the multi-parameter actuation. The extensional actuating voltage works as a buckling load, and the other two bending actuation voltages control the transverse motion of the beam, and the transition between two stable equilibrium positions.

Dano and Hyer [28] demonstrated the actuation of bistable composite laminates using shape memory alloy (SMA) wires and piezocomposite actuators. The SMA wires showed good authority although they are difficult to integrate to bistable structures.

Shultz et al. [20] achieved snap-through in a piezoelectrically actuated unsymmetric laminate in only one direction with the use of static excitation; however, very high voltages were applied to piezocomposite actuators even for a very compliant two-ply plate.

Arrieta et al. [22] and Senba et al. [23] utilized the inertial forces of bistable composites to increase the effectiveness of actuation. Arrieta et al. [22] proposed a morphing strategy based on using external energy from dynamic perturbations on the structure, resulting in dynamically triggered snap-through, although reversed snap-through was not achieved. Senba et al. [23] achieved a dynamically triggered reversed snap-through on a bistable plate using a surface-bonded piezocomposite actuator with the aid of an added mass.

Arrieta et al. [1] presented a passive load alleviation mechanism by using a bistable cross-ply laminate, which has different stiffness and dynamic characteristics for each stable state. In a follow up study, Arrieta et al. [38] used the dynamic response of a cross-ply bistable laminate to achieve a full state configuration control, capable of inducing and reversing snap-through. Bilgen et al. [2] applied the resonant control technique to a bistable cross-ply composite plate with surface-bonded piezoelectric actuators and evaluated the control effectiveness under aerodynamic loading in a wind tunnel. An analytical model was also presented for the dynamic response of a cantilevered wing-shaped bistable composite by Arrieta et al. [17].

1.1.5. Solution Methods

The dynamical behavior of different structures such as beams, plates and shells, are modeled using different differential equations. Figure 1-4 represents the most

frequently used solution methods in the area of structural dynamics for solving these mathematical models.

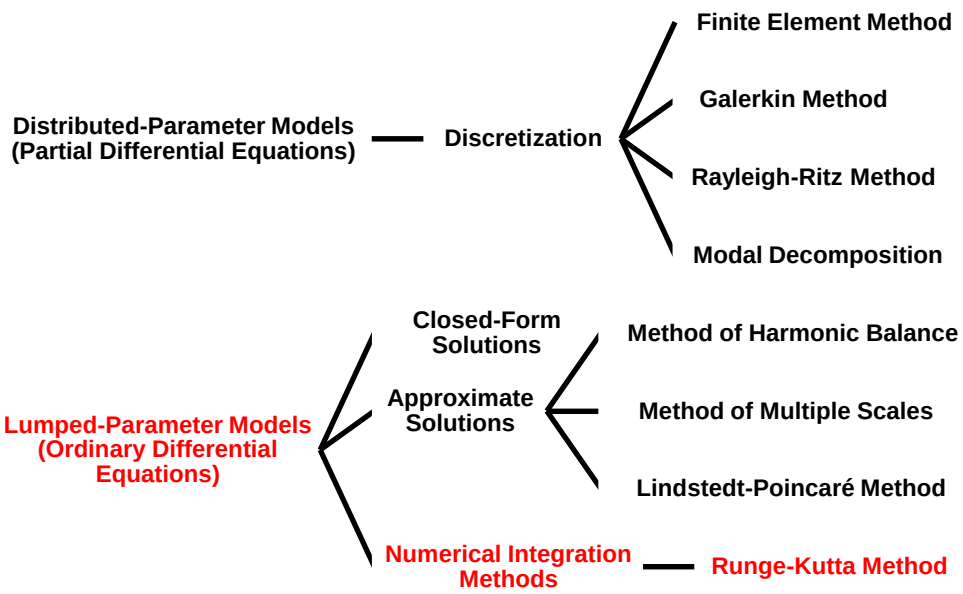

Figure 1-4. Solution methods for mathematical models of different structures.

Structures are distributed-parameter systems and constitute an infinite number of particles. As a result, a partial differential equation is used to precisely describe the dynamical behavior of a structure in time and space. In most cases, an analytical solution does not exist for a partial differential equation due to the nonlinearity in the equation or the complexity of boundary conditions.

Discretization methods are employed to solve partial differential equations with no analytical solutions. The idea is to discretize a partial differential equation into a set of ordinary differential equations. The most well-known discretization methods are the Finite Element method, the Galerkin method, the Rayleigh-Ritz method, and Modal Decomposition.

The Finite Element method subdivides a structure into smaller elements. Elements can have various shapes based on the shape of structure. Each element has a specific number of nodes, and each node has a determined degrees of freedom. For instance, a node in a beam can have degrees of freedom such as horizontal displacement, vertical displacement, and in-plane rotation. Ordinary differential equations are used to describe the dynamics of variables for each node. These differential equations are solved simultaneously to find the overall behavior of a structure. The model predicts the structure response more accurately by increasing the number of elements. The Finite Element method is the most popular numerical discretization method and is used in several commercial tools, such as ANSYS, NASTRAN, and ABACUS to name a few. The remaining methods, the Galerkin method, the Rayleigh-Ritz method, and Modal Decomposition, also converts a continuous problem into a discrete one by assuming series-type solutions with known functions for the degrees of freedom.

Another approach to describe a structure is using a lumped-parameter model. A lumped-parameter model simplifies the modeling of a spatially distributed structure by making an assumption that the structure behavior can be described using a topology with lumped values for mass, damping, and stiffness. The solution methods for a lumped-parameter model are shown in Figure 1-4.

As mentioned, this research focuses on the constrained-energy actuation of a bistable structure. However, application of bistable structures is not limited to actuation purposes as they have been proposed for harvesting vibrational energy [39, 40]. Dynamical behavior of bistable structures is usually described by employing a lumped-parameter, one-degree-of-freedom Duffing-Holmes oscillator as a governing equation [41]. The Duffing-Holmes equation has a nonlinear restoring force, consisting of linear softening and cubic hardening stiffness coefficients, that creates the bistability property. Analytical and numerical solution methods are used to solve this nonlinear ordinary

differential equation, as can be seen in Figure 1-4. The most frequently used approximate analytical solutions are method of harmonic balance and perturbation methods such as the Lindstedt-Poincaré method and the method of multiple scales [42-44]. Also, the Runge-Kutta numerical integration method is a known time-domain method to solve differential equations.

The method of harmonic balance assumes that the system response is composed of a number of harmonic terms. This method is specifically used to find the steady state response of a nonlinear ordinary differential equation subjected to a harmonic excitation. The accuracy of this method increases by increasing the number of harmonics.

The other method to solve a nonlinear differential equation analytically is using perturbation methods. Perturbation methods yield a precise equation for vibrations with low amplitude around the equilibrium position, and they become less accurate for vibrations with large amplitudes. As an example, the method of multiple scales assumes a series-type solution for the equation. The terms in the solution have different time scales, including slow-scale and fast-scale terms.

Numerical integration is the most straightforward computational method for time-domain simulations, and they are capable of finding a system response subjected to arbitrary input excitations. The Runge-Kutta numerical integration method is mostly employed to solve time-domain nonlinear differential equations in commercial software such as MATLAB [45].

Transient response is critical in studying the minimum energy actuation of a bistable structure because snap-through occurs in the transient region of the system response. As a result, numerical integration is used to solve the Duffing-Holmes equation in this dissertation since it gives both the transient and steady state responses.

1.2. Motivation

Large loads due to fluid solid interaction can lead to high bending stresses and fatigue failure in wings and wind turbine blades [18]. An appropriate solution for the mentioned problems is using a morphing bistable composite laminate for load alleviation. A bistable composite laminate is capable of attaining two statically stable shapes, and it can be designed to alleviate a critical load, such as wind gust, by snapping from one stable position to the other. For instance, Figure 1-1 shows an experimental bistable piezocomposite plate clamped at one end to form a low-aspect-ratio wing, previously proposed by Arrieta et al. [17] and Bilgen et al. [2]. The plate is made out of unsymmetrical cross-ply composite laminate designed to be bistable by locking in residual stresses during the elevated-temperature curing process. The wing has a span of 240 mm, root chord of 190 mm, and tip chord of 139 mm. Two MFC M8557-P1 type actuators are bonded near the base of the bistable wing and are oriented at 0° with respect to the span axis. This wing is bistable and capable of load alleviation. Piezocomposite actuators are used to reverse the snap-through and bring back the structure to its original optimal aerodynamic shape after the gust load is alleviated. However, there is a limit on the size of the used piezocomposite actuator, so a severe force and energy constraints exist to achieve snap-through in a morphing wing, airfoil or a wind turbine blade. In this context, the research goal is to understand how to cause a bistable structure to switch its position from one stable equilibrium position to the other in energy and force limited scenario. The bistable wing is a starting point for this research; however, the analysis is conducted so that the energy-based characteristics of a bistable structure can be understood in general (as approximated by a Duffing-type oscillator.)

1.3. Objectives

The broad goal of this research is to investigate the minimum required energy for performing snap-through of a bistable structure [46, 47].

The first objective is to mathematically model a bistable structure. The well-known one-degree-of-freedom Duffing-Holmes equation is used for this purpose. Then, the mathematical model is validated by building and testing a magneto-elastic beam subjected to harmonic excitation.

The second objective is to investigate the required energy for performing the snap-through of a bistable structure. The required energy is calculated by solving the non-linear Duffing-Holmes equation subjected to single-tone harmonic excitation and noise. The energy for performing the snap-through of the experimental bistable beam is deduced from the tests.

1.4. Outline of the Dissertation

Chapter 2 presents the mathematical modeling of a bistable structure. The dynamical behavior of a bistable structure is studied using a one-degree-of-freedom Duffing-Holmes oscillator. Next, the mathematical model is validated experimentally, using a cantilevered magneto-elastic bistable beam. Also, the energy calculation scheme for the cross-well actuation of a bistable structure is presented.

Chapter 3 presents the energy required for the cross-well actuation of a bistable structure subjected to single-tone harmonic excitation. The energy is presented as a function of excitation frequency and damping ratio for different harmonic force amplitudes. The experimental results of the bistable beam subjected to single-tone harmonic excitation are provided.

Chapter 4 presents the energy required for the cross-well actuation of the bistable structure subjected to a single-tone harmonic signal and band-limited white noise. Experimental results for single-tone harmonic excitation and noise are presented.

Chapter 5 provides a summary of the results from this research. The publications stemming from the research are listed, and a discussion of recommendations and future work is presented.

CHAPTER 2

THE DYNAMICS OF A BISTABLE STRUCTURE

2.1. Introduction

This chapter discusses the mathematical modeling of a bistable structure. The objective of this chapter is to describe the dynamical behavior of a bistable structure using a one-degree-of-freedom Duffing-Holmes oscillator and validate the mathematical model experimentally. Section 2.2 presents the mathematical modeling of a bistable structure. Section 2.3 presents the energy calculation scheme for the cross-well actuation of a bistable structure and validation of the used numerical integration method. Section 2.4 presents experimental results for a bistable beam subjected to harmonic excitation. Finally, Section 2.5 presents the conclusions of this chapter.

2.2. Mathematical Modeling

In this section, the vibration of a one-degree-of-freedom bistable structure is modeled using a Duffing-Holmes equation. Figure 2-1 shows the assumed mechanical representation of the system.

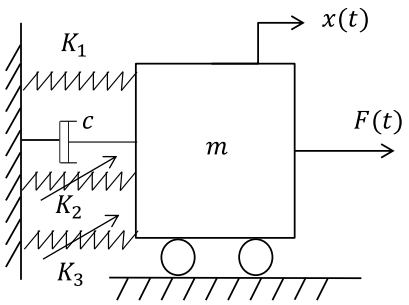

Figure 2-1. Mechanical representation of a Duffing-Holmes oscillator.

In the figure, m is the mass, c is the viscous damping coefficient, k_1 is the linear stiffness coefficient, k_2 and k_3 are nonlinear stiffness coefficients, and $x(t)$ is the displacement. The kinetic energy (T), potential energy (U), and dissipative energy (R) of such a system are described below. The over-dot denotes derivative with respect to time.

$$T = \frac{1}{2}m\dot{x}^2 \tag{2-1}$$

$$U(x) = -\frac{1}{2}k_1x^2 + \frac{1}{3}k_2x^3 + \frac{1}{4}k_3x^4 \tag{2-2}$$

$$R = \frac{1}{2}c\dot{x}^2 \tag{2-3}$$

The governing equation of a Duffing-Holmes oscillator can be derived by using the aforementioned energy relations in the Lagrange equation as follows

$$\frac{d}{dt}\left(\frac{\partial L}{\partial \dot{x}}\right) - \frac{\partial L}{\partial x} + \frac{\partial R}{\partial x} = F(t). \tag{2-4}$$

In the above equation, $F(t)$ is the actuation force, assumed to be proportional to the piezoelectric excitation voltage, where the excitation voltage is harmonic and $L = T - U$. By inserting the energy relations in Eq. (2-4) and taking the derivative of L

with respect to displacement and velocity, the governing equation of motion is calculated as:

$$m\ddot{x} + c\dot{x} - k_1 x + k_2 x^2 + k_3 x^3 = F(t). \tag{2-5}$$

or as

$$\ddot{x} + 2\zeta\omega_n\dot{x} - \omega_n^2 x + \frac{k_2}{m}x^2 + \frac{k_3}{m}x^3 = f(t). \tag{2-6}$$

when normalized by mass, where ζ is the damping ratio, ω_n is the natural frequency and f is the mass-normalized force amplitude. The restoring force, used in Eq. (2-6), corresponds to an asymmetric potential energy function. Potential energy function is symmetric when $k_2 = 0$. By solving $\frac{dU(x)}{dx} = 0$ for a symmetric potential energy function, the stable equilibrium positions are obtained as:

$$x_0 = \pm\sqrt{\frac{k_1}{k_3}} = \pm\sqrt{\frac{1}{\delta}}. \tag{2-7}$$

The non-linear-to-linear stiffness coefficient is defined as $\delta = k_3/k_1$. Figure 2-2 represents symmetric ($k_2 = 0$) and asymmetric potential energy functions, which have the same linear stiffness coefficients. For illustrative purposes, the potential wells for the symmetric potential energy are assumed to be located at $\pm$10 mm and for the asymmetric potential energy are assumed to be located at -15 mm and 10 mm, respectively.

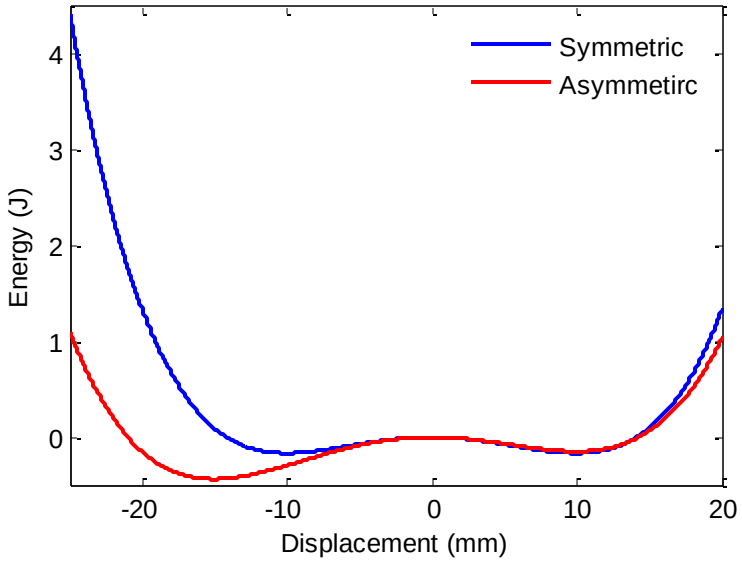

Figure 2-2. Symmetric and asymmetric potential energy functions with the same linear stiffness coefficient.

Since the objective of this research is to find the minimum energy required for moving a bistable structure from one stable equilibrium position to the other, the total energy is calculated by the integration of the product of the excitation force and velocity (V) over time, as shown in Eq. (2-8).

$$E = \int_0^{t_1} FV \, dt \tag{2-8}$$

2.3. Numerical Simulations

2.3.1. Energy Calculation Scheme

To identify the energy required for cross-well oscillation of the bistable system, as shown in Figure 1-1, the non-linear governing equation is solved for a variety of damping ratios, excitation frequencies, and force amplitudes using the Dormand-Prince numerical integration method in MATLAB implemented by the ODE45 ordinary differential equation solver. The forcing is $F(t) = F_0 \sin(\omega t)$. Static force is defined

as $F_{static} = K_1|x_0|$, where x_0 is assumed to be 10 mm. Also, F_r and ω_r are defined as the ratio of excitation force amplitude to the static force and the ratio of excitation frequency to linear natural frequency, respectively.

From previous experimental data [48], the measured natural frequencies and damping ratios corresponding to the two stable equilibrium positions of the bistable wing for State 1 are 30.5 Hz and 0.038 respectively. For State 2 they are 13.0 Hz and 0.055 respectively. It is also known that the bistable wing has asymmetric potential wells. In this chapter, the stable equilibrium positions of the bistable system are assumed to be located at $\pm$ 10 mm.

Figure 2-3 (a) shows the energy calculation scheme for a linear system, which is moved from its zero equilibrium position to 10 mm, and Figure 2-3 (b) shows the minimum energy required to move a bistable structure from its negative stable equilibrium to the unstable equilibrium.

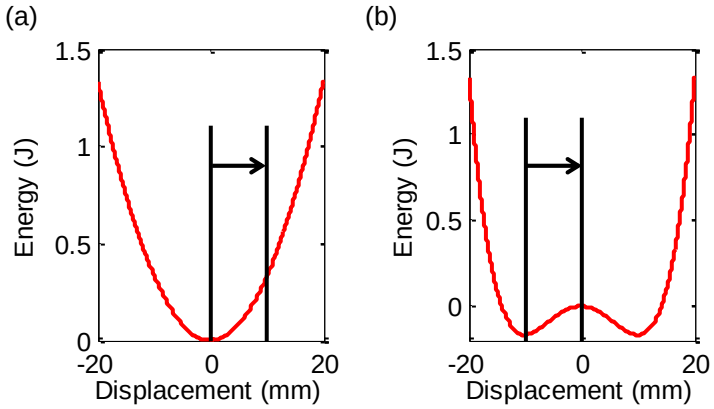

Figure 2-3. Required minimum energy for moving from the initial stable equilibrium position to the target displacement of 10 mm (a) in a linear system, and (b) in a nonlinear system.

Considering kinetic energy, the total required energy for cross-well transfer of a bistable system will be minimal if the actuator provides force slowly, minimizing losses through damping, to the system until it reaches the target position. The nonlinear

behavior of the bistable system is compared to the linear system with the same system parameters (excluding the nonlinear stiffness.) Eq. (2-9) shows the linear equation of motion, and Eq. (2-10) represents the well-known solution to that linear system subjected to a harmonic force. The solution includes the summation of two different responses: transient response and steady-state response. The transient response has an exponential decaying term, and it vanishes as time increases after which the steady-state response dominates the system response.

$$\ddot{x} + 2\zeta\omega_n\dot{x} + \omega_n^2 x = F_0 sin(\omega t) \tag{2-9}$$

$$x(t) = x_h + x_p = A\, e^{-\zeta\omega_n t}\sin(\omega_d t + \phi) + X\sin(\omega t + \theta) \tag{2-10}$$

where x_h is the solution to the homogeneous equation, and x_p is the solution to the non-homogeneous equation. The well-known amplitudes and phase angles are:

$$\begin{aligned} \mathrm{A} &= \frac{x_0 - X\sin(\theta)}{\sin(\phi)} \\ \phi &= tan^{-1}\frac{\omega_d\left(x_0 - Xsin(\theta)\right)}{\mathrm{v}_0 + \zeta\omega_n\left(x_0 - Xsin(\theta)\right) - X\omega cos(\theta)} \end{aligned} \tag{2-11}$$

$$\begin{aligned} X &= \frac{F_0/K}{\sqrt{(1-\omega_r^2)^2 + (2\zeta\omega_r)^2}} \\ \theta &= tan^{-1}\frac{-2\zeta\omega_r}{1-\omega_r^2}. \end{aligned} \tag{2-12}$$

In the above equations, x_0 and v_0 represent the initial displacement and velocity, respectively.

2.3.2. Validation of the Numerical Method

First, a linear system is solved both analytically and numerically. An example comparison of the solutions is shown in Figure 2-4 (a). As shown in the figure, the numerical and analytical solutions match. This shows the accuracy of the obtained

numerical solution. Additionally, computed analytical and numerical required energies of a linear system subjected to harmonic force of F_r= 0.25, for different excitation frequencies and damping ratios, are compared to ensure that the correct energy calculation method is used throughout the entire parameter domain. Figure 2-4 (b-c) show the analytical and numerical calculations of energy for F_r = 0.25. As can be observed, the numerical energy function matches the analytical one.

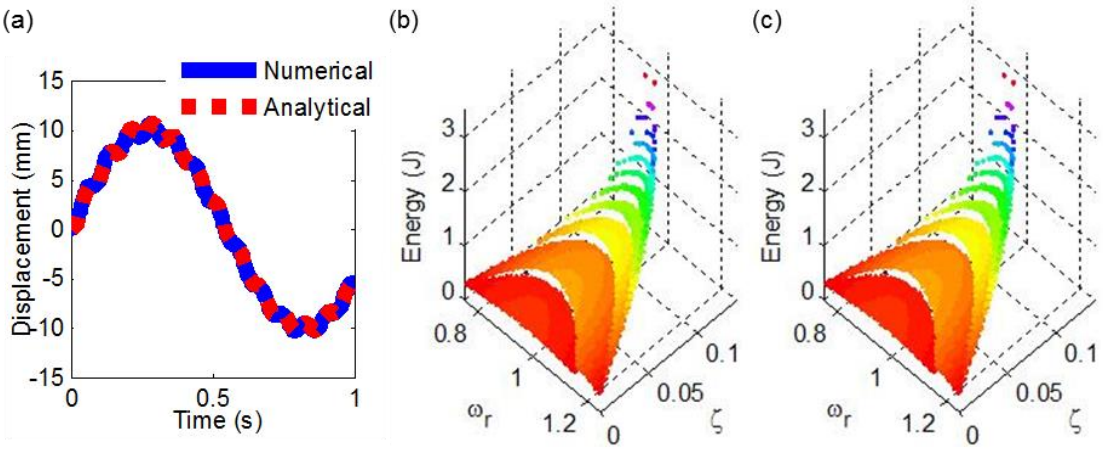

Figure 2-4. (a) Displacement vs. time for a linear system with ω_n = 13 Hz, ζ= 0.005, F_r = 1, and ω_r = 0.07 and comparison of (b) analytical energy function, (c) numerical energy function for F_r= 0.25.

2.4. Experimental Validation

2.4.1. Experimental Setup

A slender cantilevered beam with an end-mounted magnet is used as an experimental bistable structure to validate the mathematical model. A circular neodymium magnet with 12.7 mm diameter is fixed to the frame where a cubic neodymium magnet of the same size is fixed to the end of the beam. The same magnetic poles are faced toward each other to create a repulsive force, leading to a magnetically induced bistable behavior. The experimental setup is shown in Figure 2-5. The beam is

excited harmonically with a shaker and placed 41 mm away from the fixed end. A load cell, attached between the shaker and the beam, is used to measure the applied force to the beam. The beam has a rectangular cross-section, and its overhang length is 305 mm. A laser displacement sensor, located below the beam, and an accelerometer, attached on the top surface of the beam, are used to measure the transverse vibrations at 185 mm from the fixed end. The beam stable equilibrium positions are located approximately 2.9 mm above and 3.7 mm below the unstable equilibrium position, at a point where the accelerometer is located. The experiments are conducted by sweeping excitation frequency in both increasing and decreasing directions.

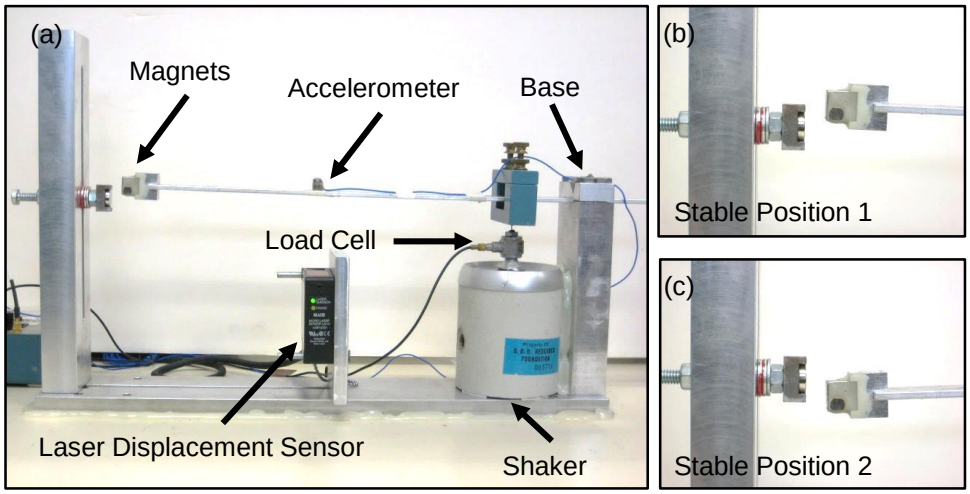

Figure 2-5. The magneto-elastic cantilevered beam: a) test apparatus, and stable equilibrium states b) One and c) Two.

A National Instruments (NI) data acquisition system is used to examine the mechanical responses of the cantilevered bistable beam. The control signal for the shaker is produced by an NI 9269 cDAQ module with 16 bit resolution (set to +/- 10 V range) at a generation rate of 2 kHz. The beam was excited for 30 cycles in order to minimize the effect of transient motion at each frequency, and the bistable beam responses during the last 20 cycles are recorded. The frequency is swept in a 12-24 Hz

band in both increasing and decreasing directions. Also, the frequency is incremented in steps of 0.05 Hz to ensure the continuity of waveform between each frequency step; therefore, the disturbance (e.g. rapid accelerations) to the beam is minimized. All experiments were conducted without removing the beam from the clamp. As a result, consistent boundary conditions were achieved. The signals of interest are measured using a NI 9239 cDAQ module with 16 bit resolution (set to +/- 10 V range). Three measured signals are: the load cell output (PCB 208B02); the laser displacement sensor output (LM10 ANR12501, with 1 μm resolution), which measures the transverse displacement of the mid-line of the beam at 185 mm from the fixed end; and the output of the accelerometer (PCB Piezotronics U352B10.)

In order to compare theoretical frequency response to the experimental one, the ratio of beam response to a specific force input should be calculated; however, the force input to the beam and the beam displacement and acceleration responses are measured at different locations, as shown in Figure 2-5 (a). The displacement and acceleration responses at the location of load cell can be found by multiplying the mentioned responses by a geometric correction factor. The geometric correction factor is the ratio of deflection at the load cell location to the deflection of the beam at the point where the accelerometer is located. This correction factor is calculated by approximating that the beam is vibrating in the first mode, and its transverse displacement distribution can be found using Euler-Bernoulli beam theory. The assumed geometric correction factor is 0.1637, which was found by using the obtained transverse deflection formula for a cantilever beam subjected to a point load. Figure 2-6 shows a cantilevered beam subjected to a point load. Also, the transverse distribution along the beam length is shown in Eq. (2-13).

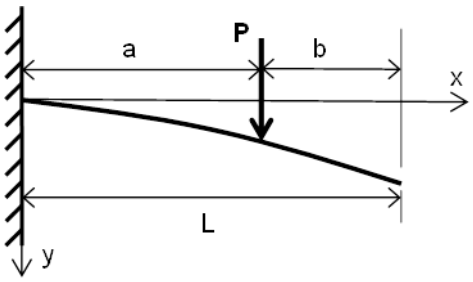

Figure 2-6. A cantilevered beam subjected to a point load.

$$y = \frac{Px^2}{6EI}(3a - x) \ldots\ldots 0 < x < a$$
$$y = \frac{Px^2}{6EI}(3x - a) \ldots\ldots \mathrm{a} < x < L \qquad (2\text{-}13)$$

First, the linear beam parameters are identified by measuring the beam frequency response without using any magnets. The identified parameters are effective mass, linear stiffness, and damping ratio. These parameters are used in the nonlinear system equation to predict the bistable beam frequency response. The comparison between experimental and predicted numerical results is presented in the next section.

2.4.2. Experimental Results

Table 2-1 shows the identified parameters for the linear beam and the coefficients used in the Duffing-Holmes equation to predict the behavior of the bistable beam. The bistable beam was initially located at the top stable equilibrium, 2.9 mm, before the frequency sweep started. It is approximated that the stable equilibrium positions are located symmetrically at 2.9 mm below and above the unstable position at the location of the accelerometer due to employing the symmetric potential energy function to find the nonlinear restoring force in the Duffing-Holmes equation. The approximated stable equilibrium positions are multiplied by the geometric correction factor to yield the locations of stable equilibriums at the position of the load cell. Then, the nonlinear stiffness coefficient, k_3, is obtained by using Eq. (2-7).

Table 2-1. Identified linear beam parameters and parameters used for the bistable beam.

Parameter	Linear System	Bistable System
m (kg)	16.5	16.5
k_1 (N/m)	$1.77*10^5$	$-1.59*10^5$
k_3 (N/m)	0	$7.10*10^{11}$
ζ	0.006	0.125

As represented in Table 2-1, the bistable system linear stiffness and damping ratios are different from the identified ones for the linear system. The linear stiffness was corrected by a factor of 0.9 because the obtained theoretical frequency response underpredicts the frequency where the jump phenomenon occurs by using the identified linear stiffness. Also, the damping ratio was increased to decrease the discrepancy between theoretical and experimental frequency responses of the bistable beam. The bistable system was simulated with initial displacement at the top stable position and zero initial velocity for 200 cycles at each frequency. The system time response in the last 25 cycles was used to calculate the frequency response.

Figure 2-7 (a-b) present the ratio of displacement standard deviation (STD) to force STD and the ratio of acceleration STD to force STD.

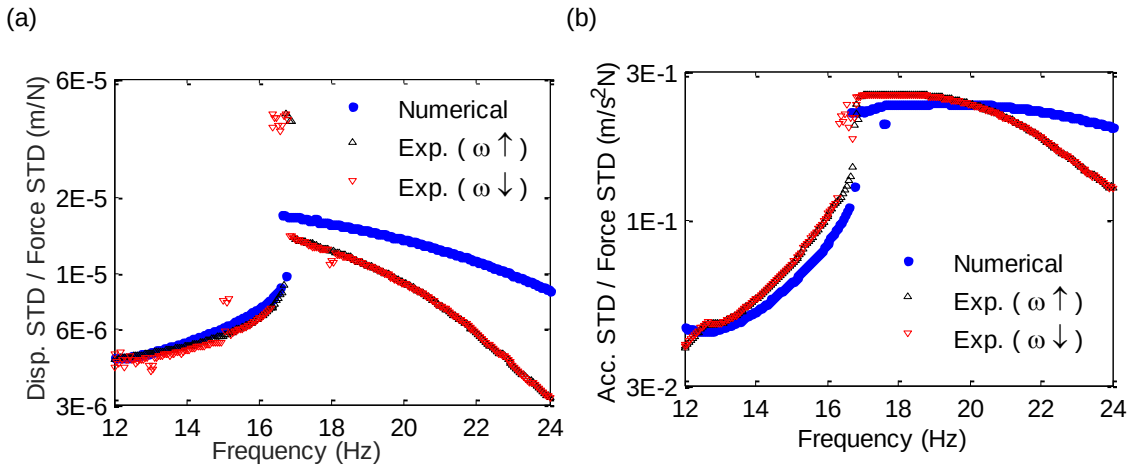

Figure 2-7. Numerical and experimental frequency responses: (a) displacement standard deviation to force standard deviation (b) acceleration standard deviation to force standard deviation.

As represented in Figure 2-7 (a), a good match exists between the experimental and the numerical frequency responses below the frequency of 16.7 Hz where the jump phenomenon occurs. The numerical model overpredicts the system response for the frequencies higher than the jump phenomenon frequency. Also, the numerical model does not predict a few isolated experimental points with a large displacement to force ratio in the 16.75-16.85 Hz band.

The acceleration frequency responses are shown in Figure 2-7 (b). A small mismatch exists between the numerical and the experimental acceleration frequency responses in the whole frequency band, and the mismatch is specifically larger for frequencies higher than 21 Hz. As observed in Figure 2-7 (a-b), the theoretical model predicts the bistable beam frequency responses with an acceptable accuracy although discrepancies exist between the experimental and the numerical results, specifically at high frequencies. This is expected because the beam is a distributed parameter system, and it is reasonable to assume that the second and third modes have a measurable effect on the beam near its first mode.

Phase portraits with Poincaré points are plotted to check the dynamical behavior for the bistable beam at different frequencies. Figure 2-8 represents numerical and experimental phase portraits at 16.8 Hz.

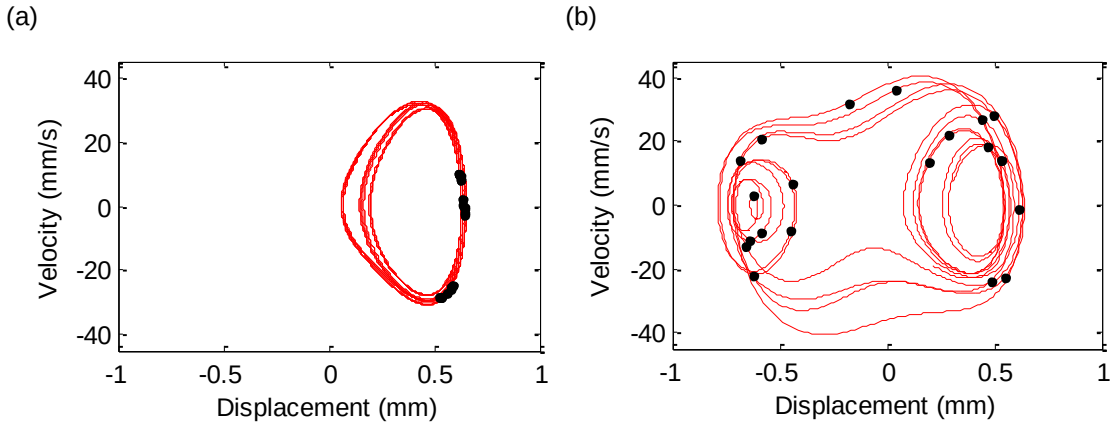

Figure 2-8. Phase portraits at the frequency of 16.8 Hz: (a) numerical (b) experimental.

As can be observed in Figure 2-8 (a), the theoretical model predicts a single-well oscillation for the system although the bistable beam is oscillating back and forth between two potential wells, as shown in Figure 2-8 (b). The system response at this frequency belongs to the few isolated points located in Figure 2-7 (a). As expected, it seems that the theoretical model is not able to predict the exact dynamical behavior at this frequency and the other points in 16.75-16.85 Hz band. Phase portraits are also plotted at three other frequencies. Figure 2-9 shows the numerical and the experimental phase portraits at the frequencies of 14, 17 and 22 Hz. These frequencies are selected from three different points in the entire frequency range and are far from each other.

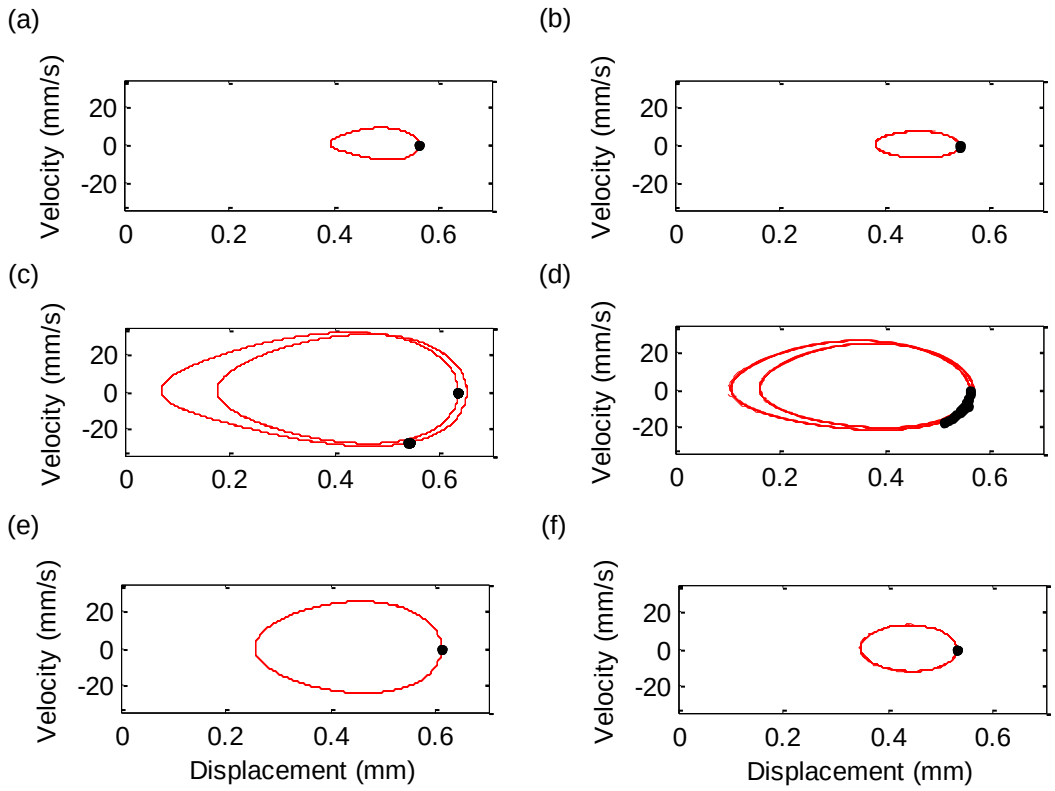

Figure 2-9. Phase portraits at the frequency of 14 Hz: (a) numerical (b) experimental; 17 Hz: (c) numerical (d) experimental; 22 Hz: (e) numerical (f) experimental (equal horizontal scale for all plots).

As represented in Figure 2-9 (a-b), both numerical and experimental results predict a period-one single well oscillation at 14 Hz. The experimental and numerical phase portraits in Figure 2-9 (c-d) are very similar, but they appear to have different Poincaré points. This is mainly because the sampling rate for the numerical simulation (100 kHz) is much larger than the experimental sampling rate (2000 Hz). Both phase portraits in Figure 2-9 (e-f) demonstrate single-well periodic oscillation, but the numerical model overpredicts displacement and velocity amplitudes. As observed in Figure 2-9, the theoretical model predicts correct time responses in the entire frequency range except for a few frequencies in 16.75-16.85 Hz range.

A displacement bifurcation diagram can be plotted to obtain an overall picture of the bistable system behavior in the entire frequency range. Figure 2-10 shows the

numerical and the experimental displacement bifurcation diagrams, which are sampled displacement responses at different frequencies.

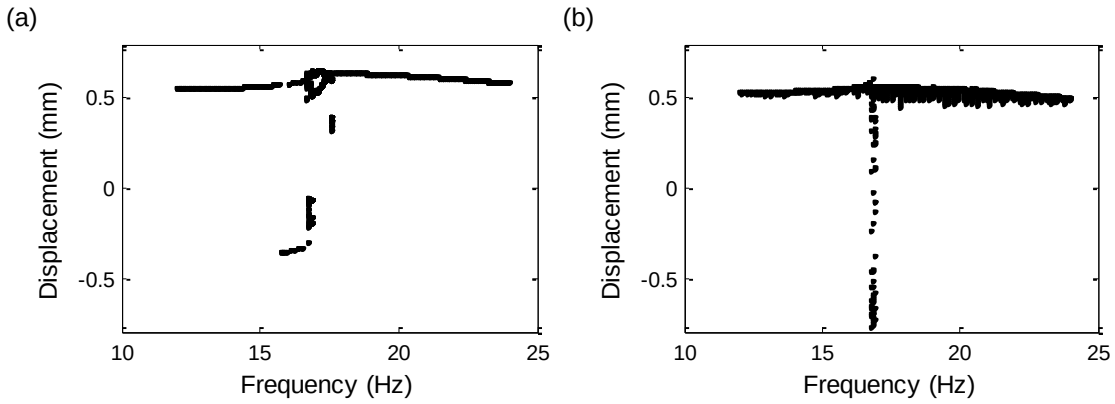

Figure 2-10. Bifurcation diagrams from: (a) numerical and (b) experimental results.

Figure 2-10 (a) shows the numerical bifurcation diagram. The system has periodic solutions in the entire range except at the frequencies close to 16.7 Hz where multiple responses, including negative values, exist at a single frequency. This means that the system may have periodic responses with a period larger than the excitation frequency, and the system snaps from a positive stable equilibrium to a negative one. Figure 2-10 (b) represents the experimental bifurcation diagram. As can be seen, experimental and numerical results look very similar, except at the frequencies around 16.7 Hz. This was demonstrated earlier as the numerical frequency results did not predict correct dynamical behavior for a few frequencies in the 16.75-16.85 Hz range. Apart from 16.7 Hz in the experimental bifurcation diagram, the sampled responses look like small blocks of dots that get wider at higher frequencies. This mainly results from the fact that the experimental time resolution is not small enough to predict sampled responses precisely, so sampled responses appear to fluctuate instead of being a single line. This is not seen in the numerical bifurcation diagram since a time

resolution of 10^{-5} s was used. Figure 2-11 represents numerical bifurcation diagrams for different damping ratios.

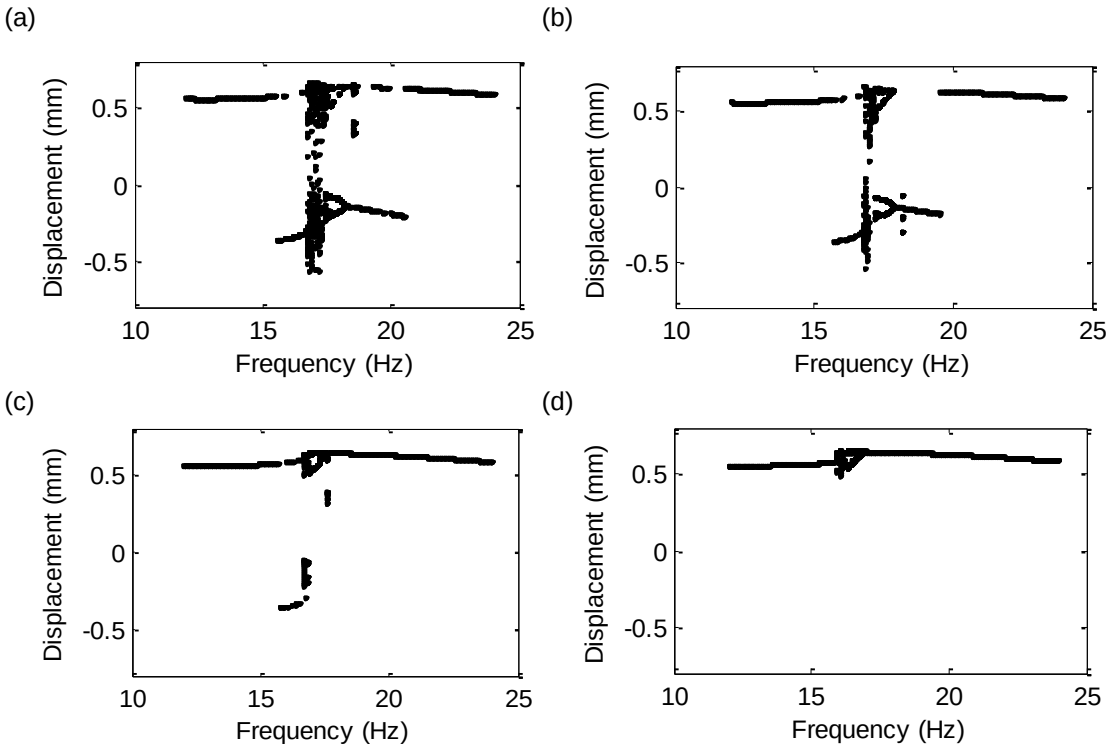

Figure 2-11. Numerical bifurcation diagrams for the damping ratios of: (a) 0.11 (b) 0.12, (c) 0.125 (d) 0.135.

Figure 2-11 is presented to explain why a damping ratio of 0.12 was selected for numerical calculation of frequency response. As can be observed in Figure 2-11 (a), there is a large frequency band where the system is doing cross-well oscillation for damping ratios less than 0.12. The number of points capable of doing cross-well oscillation decreases by increasing the damping ratio from 0.11 to 0.135 in Figure 2-11 (b-d). There is no point capable of doing cross-well oscillation in the entire frequency range for the damping ratio of 0.135, as represented in Figure 2-11 (d). Figure 2-11 highlights the sensitivity of the bistable system to damping ratio and also shows that a proper value was estimated for modeling the system.

Overall, there is a good match between predicted numerical results and experimental frequency responses. A number of important issues exist that are responsible for the discrepancy between experimental and numerical results. First, a mathematical model with symmetric potential wells was used to model the experimental response although it is known that the bistable beam potential wells are located asymmetrically around the unstable position. Second, a one-degree-of-freedom model is used for the bistable beam by assuming that the bistable beam is vibrating in the first mode. The differences between numerical and experimental results increase at higher frequencies as the contributions from higher modes of the motion increase at these frequencies, so a single-mode vibration assumption creates differences between numerical and experimental results when the bistable beam has other modes of vibration in addition to the first mode.

Based on the comparison between the numerical and the experimental results, it is verified that the Duffing-Holmes equation is able to predict the response of a bistable structure. Therefore, the cross-well actuation energy analysis is presented in the next chapter by solving this nonlinear equation for different parameters.

2.5. Conclusions

In this chapter, the dynamical behavior of a bistable structure is modeled using the one-degree-of-freedom Duffing-Holmes oscillator. Experiments are conducted on a bistable beam to validate the mathematical model. Experimental and theoretical frequency responses, including the ratios of displacement to force and acceleration to force, are compared to each other. In addition, experimental and theoretical phase portraits are plotted to determine whether a correct dynamical behavior is predicted by the mathematical model at different frequencies. A good match exists between theoretical and experimental results.

CHAPTER 3

SINGLE-TONE HARMONIC EXCITATION

3.1. Introduction

This chapter seeks to understand how the required energy for cross-well oscillation varies by changing damping ratio and excitation frequency for different values of excitation force amplitudes. The excitation considered is a single-tone harmonic signal. Parameter values for studying the required energy for cross-well actuation are presented in Section 3.2. Section 3.3 presents energy functions for the linear system subjected to different force amplitudes. Section 3.4 presents energy results for the bistable structure. The energy functions for linear and bistable systems are compared in Section 3.5. Conclusions are presented in Section 3.6.

3.2. Parametric Analysis Method

Three different force amplitudes are considered: one quarter of the static force, equivalent to the static force, and 1.5 times the static force. It is re-emphasized that this research considers a generic bistable system represented by the Duffing-Holmes oscillator. As a result, the exact kinematic or distributed-parameter nature of the system is not of concern. Table 3-1 shows the range of parameters used for numerical simulations.

Table 3-1. Parameters for numerical simulations.

Parameter	Range
m (kg)	1.00
ω_n (Hz)	13.0
ζ	0 - 1
k_1 (N/m)	ω_n^2
δ	$1.00*10^4$
k_3 (N/m)	$6.67*10^3$
$F_r = F_0/F_{static}$	0.250,1.00, 1.50
$\omega_r = \omega/\omega_n$	0 - 10

3.3. Linear System Energy Behavior

3.3.1. Force Ratio of 0.25

Figure 3-1 shows the minimum energy required for moving the linear system with a harmonic excitation force amplitude equivalent to the one-fourth of static force from its zero equilibrium position to the target displacement of 10 mm.

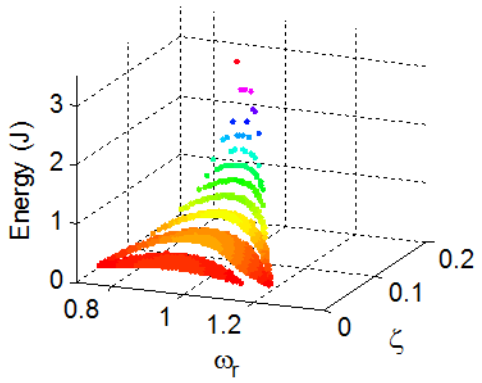

Figure 3-1. Total energy of an under-actuated linear system with F_r = 0.25 as a function of frequency ratio and damping ratio.

The energy function in Figure 3-1 is divided into several levels. If the excitation frequency is close to the natural frequency, the linear system can reach the target

displacement in the transient region of the response in a various number of cycles, which creates discrete jumps in the total energy.

Figure 3-2 shows time histories of displacements for three different linear systems with the same force amplitudes and excitation frequencies but with small difference in damping ratios. As represented in the figure, three linear systems with the corresponding damping ratios of 0.115, 0.120, and 0.125 reach the target displacement of 10 mm in 6, 8, and 14 half cycles, respectively, and calculated energies are 1.27 J, 1.75 J, and 3.23 J. Figure 3-2 also shows that a small change in damping ratio results in a large change in the required energy; this is of course a consequence of the fact that the system is so-called "under-actuated" from a static sense.

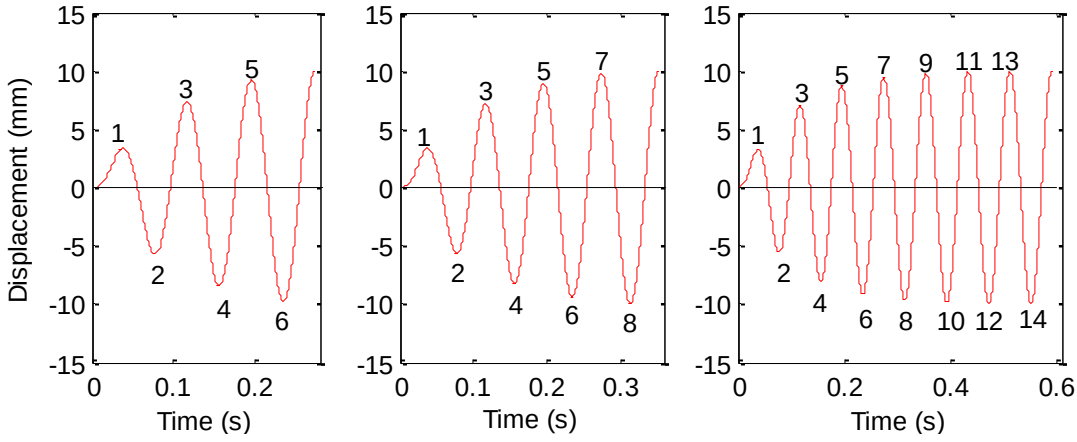

Figure 3-2. Displacement time history for the linear system until displacement reaches the target value of 10 mm with F_r = 0.25, excitation frequency ratio of 0.97, and damping ratios of (a) ζ = 0.115 (b) ζ = 0.120 (c) ζ = 0.125.

Figure 3-3 (a) presents the number of zero-velocity crossings until the system reaches the target displacement as an indication of the total time that is required to reach the objective position. Discrete energy levels are clearly identified by a discrete number of zero-velocity crossings (as indicated by labels 2, 3, 4,… in the figure.) Figure 3-3 (b) shows the number of half cycles obtained by considering excitation time period

as a cycle time period. Figure 3-3 (a-b) are not exactly the same because the number of zero-velocity crossings and the number of half cycles are different from each other. The number of zero-velocity crossings is equal to the number of peaks and valleys of the total response while the number of half cycles is found by dividing the time that it takes for a system to reach objective displacement by the excitation period. Although the number of half cycles is a more direct measure of elapsed time, it is not always applicable to the potential response of a non-linear system since a non-linear system can have a non-periodic response with the application of a periodic force. For this reason, and for consistency, the number of zero-velocity crossings is used to evaluate elapsed time with respect to excitation period.

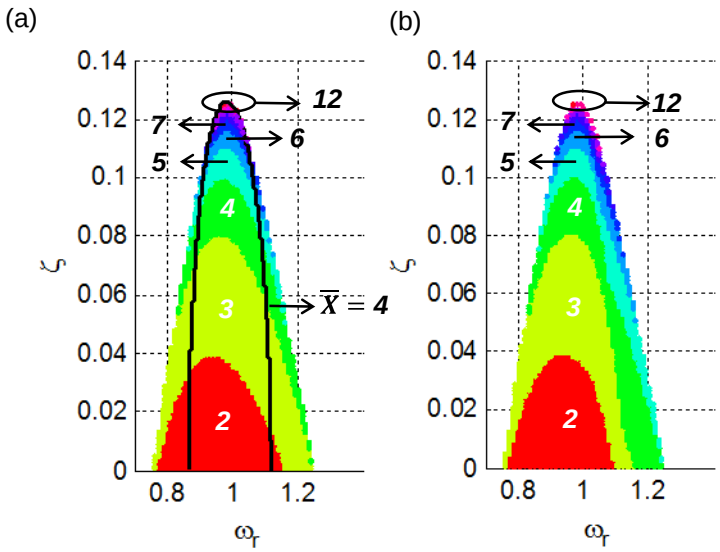

Figure 3-3. Response of an under-actuated linear system with F_r = 0.25 as a function of frequency ratio and damping ratio: (a) number of zero-velocity crossings (b) number of half cycles.

Normalized Amplitude

A normalized amplitude, $\overline{X}$, is defined as $\frac{X_0 K}{F_0}$, where F_0 is the force amplitude and X_0 is the steady state response amplitude of 10 mm. The relation between frequency ratio and damping ratio for a specific harmonic force amplitude and a steady state

response amplitude can be found by using the steady state response amplitude relation in Eq. (2-12). For any F_r and X_0 = 10 mm, $\overline{X}$ is equal to $\frac{1}{F_r}$. The relation between damping ratio and excitation frequency ratio for $\overline{X} = \frac{1}{F_r} = 4$ is found and represented in Eq. (3-1):

$$(1 - \omega_r{}^2)^2 + (2\zeta\omega_r)^2 = \frac{1}{\overline{X}^2} = \frac{1}{16} \tag{3-1}$$

The curve for $\overline{X}$ = 4 is plotted in Figure 3-3 (a) using Eq. (3-1). The points on the curve have a steady state amplitude equal to 10 mm, and the points inside the curve have steady state amplitudes larger than 10 mm. As can be observed in Figure 3-3 (a), all the points inside $\overline{X}$ = 4 are able to reach the target displacement of 10 mm. There are also sub-domains of parameters outside $\overline{X}$ = 4 where the linear system is able to reach objective displacement although the sub-domain's steady state response amplitudes are less than 10 mm. This is because the linear system reaches the target displacement in the transient region of the response, and the transient response peaks for these points are equal or larger than 10 mm. As a result, it is shown that $\overline{X}$ = 4 gives a good estimate but not a complete one for the regions of damping ratio and excitation frequency, where a linear system is able to reach the objective displacement for F_r = 0.25.

Normalized Damping Energy

Two different views of the ratio of damping energy to the total energy are plotted in Figure 3-4. The color bar in Figure 3-4 shows the color distribution proportional to the number of zero-velocity crossings at each point. As can be seen in the figures, normalized damping energy varies from zero to 88%. The normalized damping energy values are large for the regions where total energy is large because a linear system takes longer to the objective displacement when it is located in the high energy regions. Consequently, a larger amount of energy is dissipated through damping when the time increases.

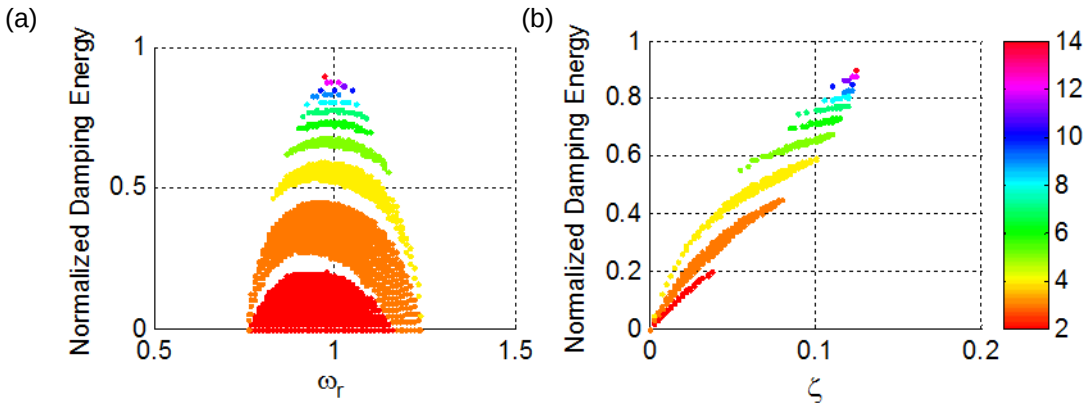

Figure 3-4. Response of an under-actuated linear system with F_r = 0.25 as a function of frequency ratio and damping ratio: (a) zero degree azimuth angle view (b) ninety degree azimuth angle view.

3.3.2. Force Ratio of 1

By equating the harmonic force amplitude to the static force, the energy function becomes less quantized. There are low energy and high energy levels in Figure 3-5 (a) separated by a line. The same line can be seen in Figure 3-5 (b). It is shown that the section of the energy function with a lower energy level (no zero-velocity crossing) reaches the unstable equilibrium point with a lower number of zero-velocity crossings, compared to the part with higher energy level (one zero-velocity crossing.) All of the points capable of reaching the objective displacement are located below the $\zeta = 0.707$ line. A linear system with a damping ratio larger than $\zeta = 0.707$ does not have a resonant peak in the frequency domain, and the system response has the maximum steady state amplitude when a static force is applied to it. Therefore, increasing excitation frequency to natural frequency does not increase the linear system response peak for damping ratios larger than $\zeta = 0.707$.

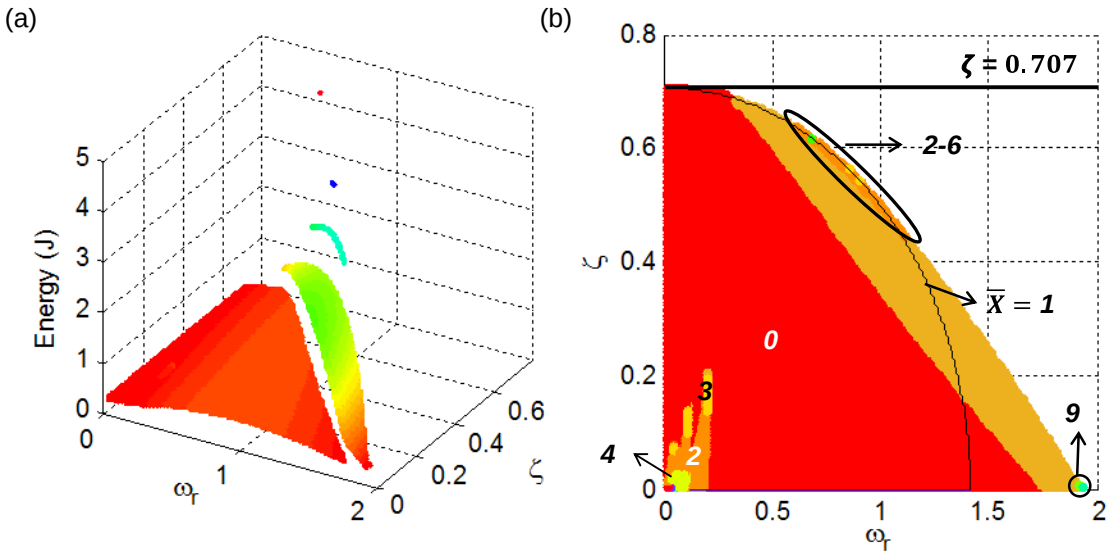

Figure 3-5. Response of a linear system with F_r = 1 as a function of frequency ratio and damping ratio: (a) Total energy, and (b) number of zero-velocity crossings.

Additionally, there is a small region in the bottom left corner of Figure 3-5 (b), where the system has a response with multiple zero-velocity crossings. For small damping ratios, the transient response decays slowly, and this creates local extrema in the system response. The velocity sign changes around these local extrema and crosses zero value. Figure 3-2 (a) shows the response of a linear system with low frequency ratio and low damping ratio, belonging to the left bottom corner region of Figure 3-5 (b). As can be seen in Figure 2-4 (a), the system has four local extrema (two minima and two maxima) until it reaches a displacement value of 10 mm, so the number of zero-velocity crossings is four although the system reaches the target displacement in a quarter of a cycle. Also, $\overline{X}$ = 1 in Figure 3-5 (b) represents linear systems that have steady state response amplitude of 10 mm for F_r = 1. All the points inside $\overline{X}$ = 1 have steady state response amplitude larger than 10 mm and are capable of reaching the target displacement.

3.3.3. Force Ratio of 1.5

Figure 3-6 shows the energy function and number of zero-velocity crossings for a linear system subjected to a harmonic excitation with amplitude that is 1.5 times the static force amplitude.

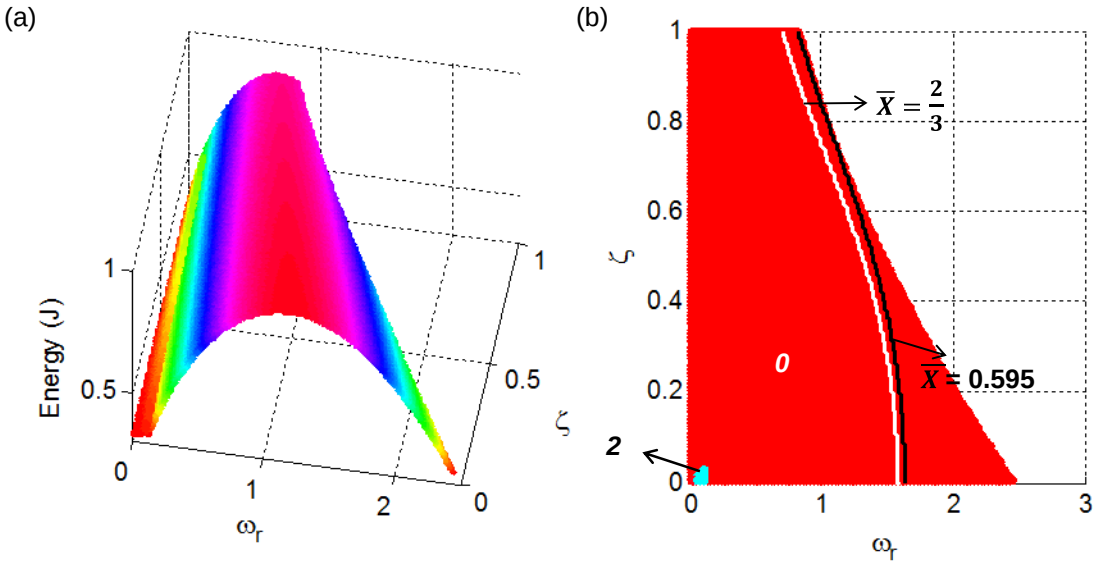

Figure 3-6. Response of a linear system with F_r =1.5 as a function of frequency ratio and damping ratio: (a) Total energy, and (b) number of zero-velocity crossings.

As expected, the energy function shows a single energy level in Figure 3-6 (a) since the excitation force amplitude is 1.5 times the static force. Here, we note the number of zero-velocity crossings is two for the bottom left corner of Figure 3-6 (b); this is the same behavior that was observed in Figure 3-5 (b). $\overline{X}$ = 0.595 (F_r = 1.68) estimates more complete ranges of damping ratio and excitation frequency, capable of reaching objective displacement, for F_r = 1.5. Finally, it is logically concluded that the jumps and discontinuities in total energy decrease by increasing the force amplitude. It is also clearly demonstrated that a statically under-actuated linear system will reach a desired displacement over time given that it is equal or below the steady-state amplitude;

however, an energy-limited (fixed-capacity) system may "run-out-of-steam" due to wasting energy towards dissipative components.

3.4. Bistable System Energy Behavior

The response of the bistable system to harmonic excitation is first investigated by plotting phase portraits of a system with different damping ratios and subjected to different harmonic force amplitudes and excitation frequencies. Figure 3-7 shows various interesting phase portraits of a bistable system having its stable equilibriums located at ± 10 mm. Figure 3-7 (a-b) show the response of an under-actuated system (F_r = 0.25). Figure 3-7 (a) represents a periodic single-well oscillation of a system with ζ = 0.25 and ω_r = 1. By decreasing ζ to 0.151 and increasing ω_r to 1.08, the system oscillates back and forth between two stable potential wells, as shown in Figure 3-7 (b). Figure 3-7 (c, e) illustrate the bistable system with the same parameters as in Figure 3-7 (a) except that it is subjected to larger force amplitudes, F_r = 1 and F_r = 1.5, respectively. The system response changes from a single-well oscillation to a periodic cross-well oscillation by increasing F_r from 0.25 to 1, as can be observed in Figure 3-7 (c). Further increasing F_r to 1.5, the system in Figure 3-7 (e) has a cross-well oscillation with larger displacement amplitude compared to cross-well oscillation shown in Figure 3-7 (c). Figure 3-7 (f) demonstrates the chaotic cross-well oscillation for the system with F_r = 1.5, ζ = 0.005 and ω_r = 2.61.

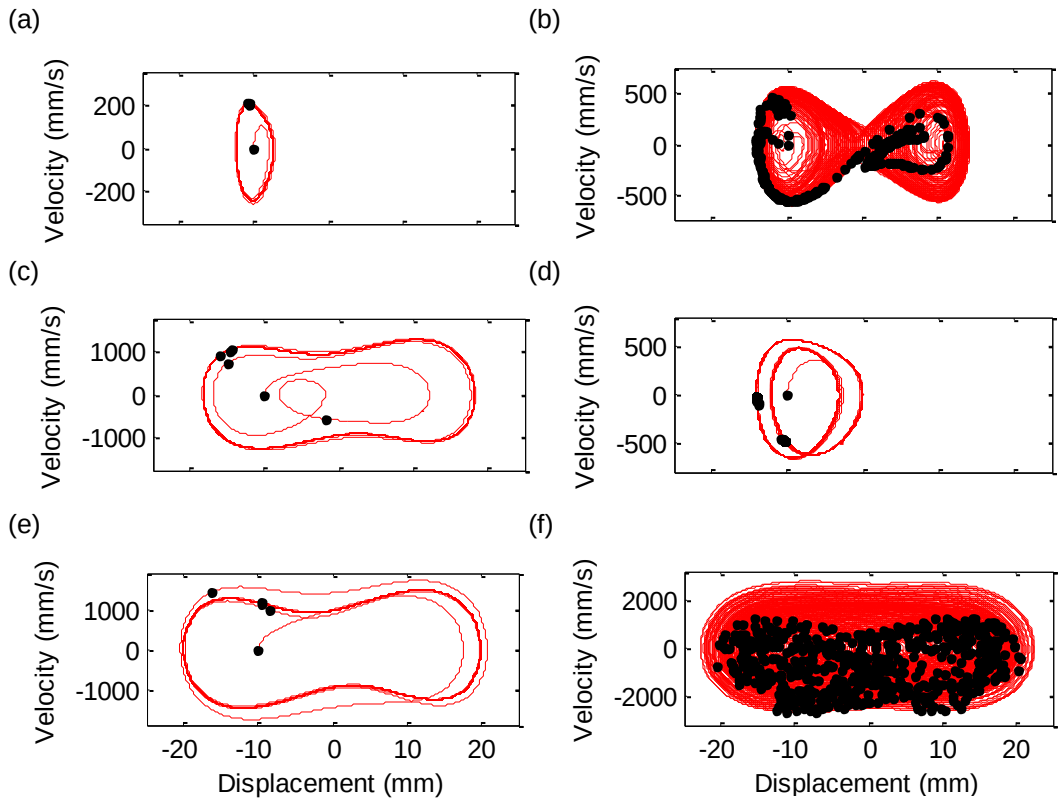

Figure 3-7. Example phase portraits of a bistable system with (a) $F_r = 0.25$, $\omega_r = 1$, $\zeta = 0.25$ (b) $F_r = 0.25$, $\omega_r = 1.08$, $\zeta = 0.151$ (c) $F_r = 1$, $\omega_r = 1$, $\zeta = 0.25$ (d) $F_r = 1$, $\omega_r = 1.23$, $\zeta = 0.605$ (e) $F_r = 1.5$, $\omega_r = 1$, $\zeta = 0.25$ (f) $F_r = 1.5$, $\omega_r = 2.61$, $\zeta = 0.005$ (equal horizontal scale for all plots).

Figure 3-7 demonstrates that a variety of types of oscillations can be achieved depending on the system parameters and forcing. The complete possibilities of response of the bistable system are parametrically studied for three different harmonic force amplitudes.

3.4.1. Force Ratio of 0.25

Figure 3-8 (a) shows the energy function for a bistable system in response to a harmonic force with the force amplitude equal to one-quarter of the static force. Additionally, Figure 3-8 (b) shows that different energy levels correspond to a discrete number of zero-velocity crossings.

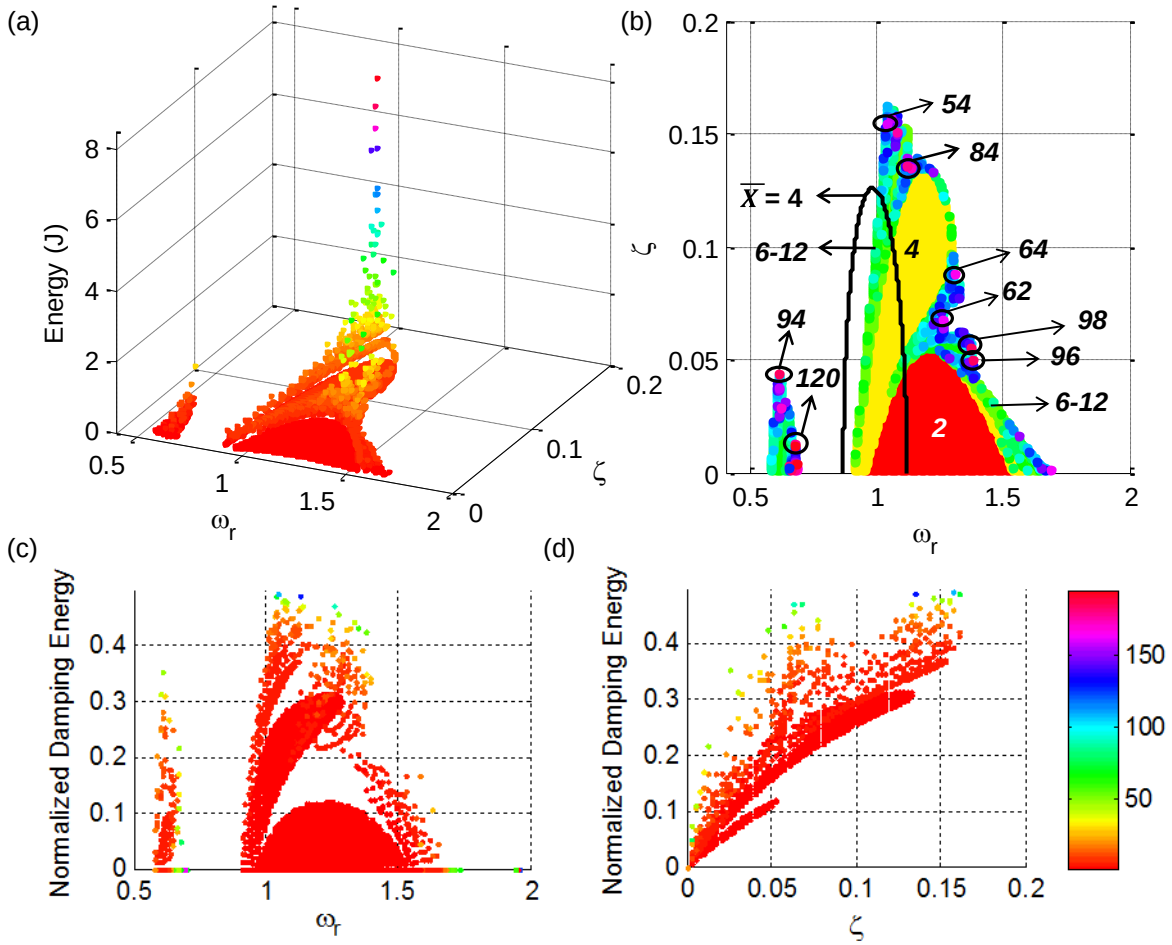

Figure 3-8. Response of an under-actuated bistable structure with F_r = 0.25 as a function of frequency ratio and damping ratio: (a) Total energy (b) number of zero-velocity crossings; normalized damping energy: (c) zero degree azimuth angle view (d) ninety degree azimuth angle view.

In most cases, for F_r = 0.25, the bistable system with damping ratio of less than 0.16 and excitation frequency ratio between 0.5 and 1.7 is able to achieve a cross-well transfer, as shown in Figure 3-8 (a). The energy is quantized into different levels, and it is also highly scattered due to the nonlinear nature of the system. For instance, there is a small region around the excitation frequency ratio of 0.6, where the bistable structure can do cross-well oscillation. $\overline{X} = 4$ was added to Figure 3-8 (b) to compare linear and bistable systems, and it can be observed that the bistable system has a different range of damping ratios and frequency ratios capable of reaching the target displacement.

Figure 3-8 (c-d) present two different views of the normalized damping energy for an under-actuated bistable structure. Maximum normalized damping energy is 48%, which is much lower compared to the under-actuated linear system with a maximum normalized damping energy of 88%. Also, damping energy is large for high levels of total energy, similar to the under-actuated linear system.

3.4.2. Force Ratio of 1

Figure 3-9 shows the response of the system subjected to the force amplitude equal to the static force. The bistable structure is able to achieve cross-well oscillation in a much wider range of excitation frequencies and damping ratios, compared to the case where force amplitude is less than the static force. Additionally, the energy levels are highly quantized for the excitation frequency ratios between 2 and 3. Using $\overline{X} = 1$ as a criterion, it can be seen that the bistable system has a wider range of damping ratios and excitation frequencies that are able to reach the target displacement, compared to the linear system subjected to the same force amplitude.

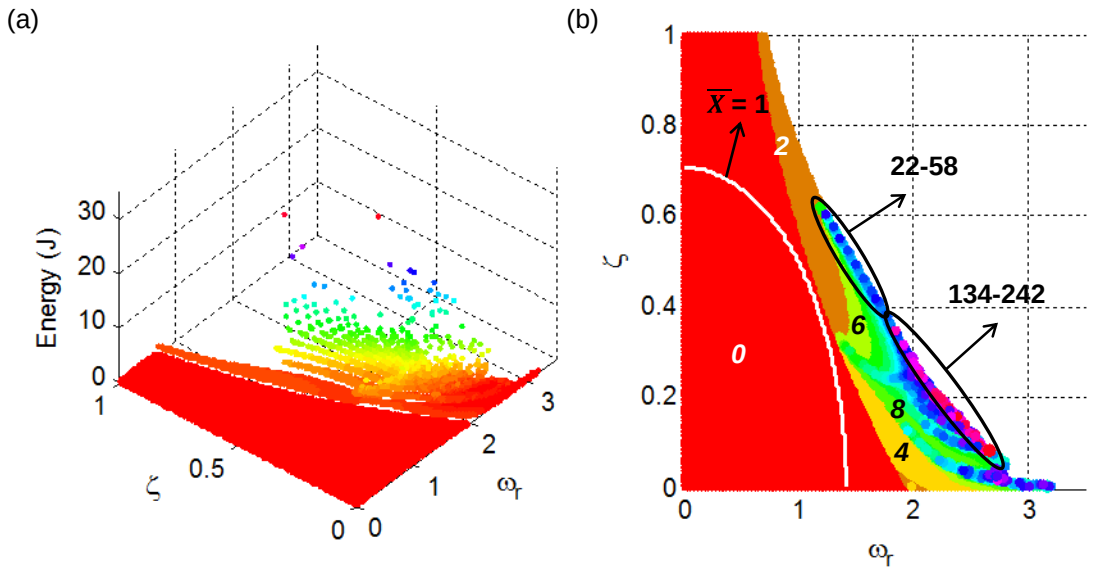

Figure 3-9. Response of a bistable structure with F_r = 1 as a function of frequency ratio and damping ratio: (a) Total energy, and (b) number of zero-velocity crossings.

3.4.3. Force Ratio of 1.5

Figure 3-10 represents the energy function of a bistable system subjected to harmonic force with $F_r = 1.5$. The energy function in Figure 3-10 (a) looks similar to the one in Figure 3-9 (a) except that the energy is less quantized for the frequency ratios between two and three. It can be observed in Figures 3-6 to 3-8 that the energy function becomes more continuous and the range of damping ratio and excitation frequency ratio, capable of achieving cross-well oscillation, increase by increasing the force amplitude. The bistable structure response shown in Figure 3-10 has a larger range of damping ratio and excitation frequency compared to the linear system response shown in Figure 3-6, which can also be seen by checking $\overline{X} = \frac{2}{3}$ in both figures.

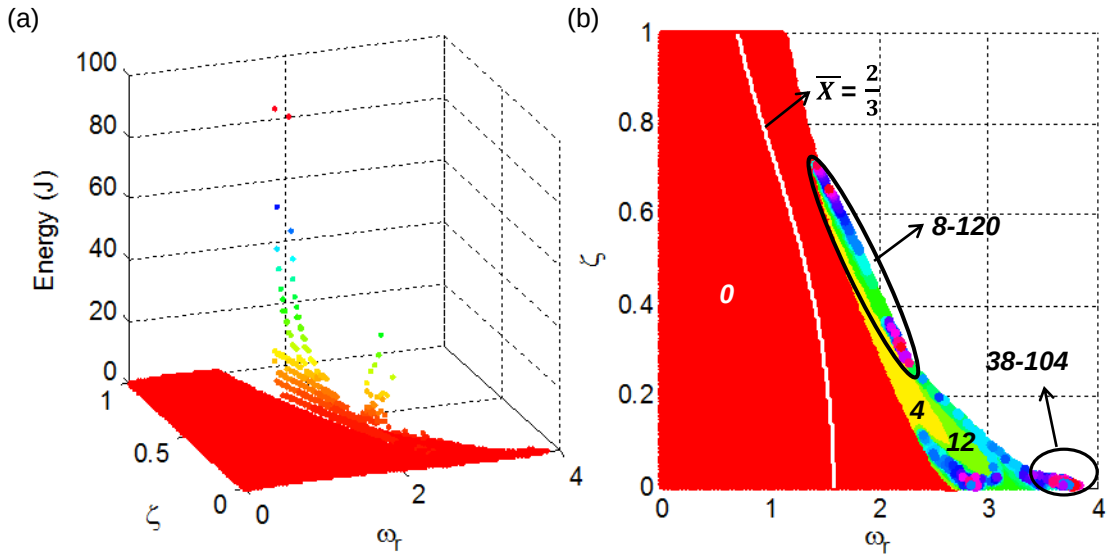

Figure 3-10. Response of a bistable structure with F_r = 1.5 as a function of frequency ratio and damping ratio: (a) Total energy, and (b) number of zero-velocity crossings.

3.5. Comparison of the Linear and the Non-Linear Systems

For F_r = 0.25, a linear system has an energy function that is divided into several levels, and a bistable structure has a scattered energy function with a small disconnected region around an excitation frequency ratio of 0.6. Figure 3-11 presents the number of zero-velocity crossings of the linear and the bistable systems subjected to F_r = 0.25. The under-actuated bistable structure has different ranges of excitation frequency and damping ratio when compared to the linear system subjected to the same force amplitude.

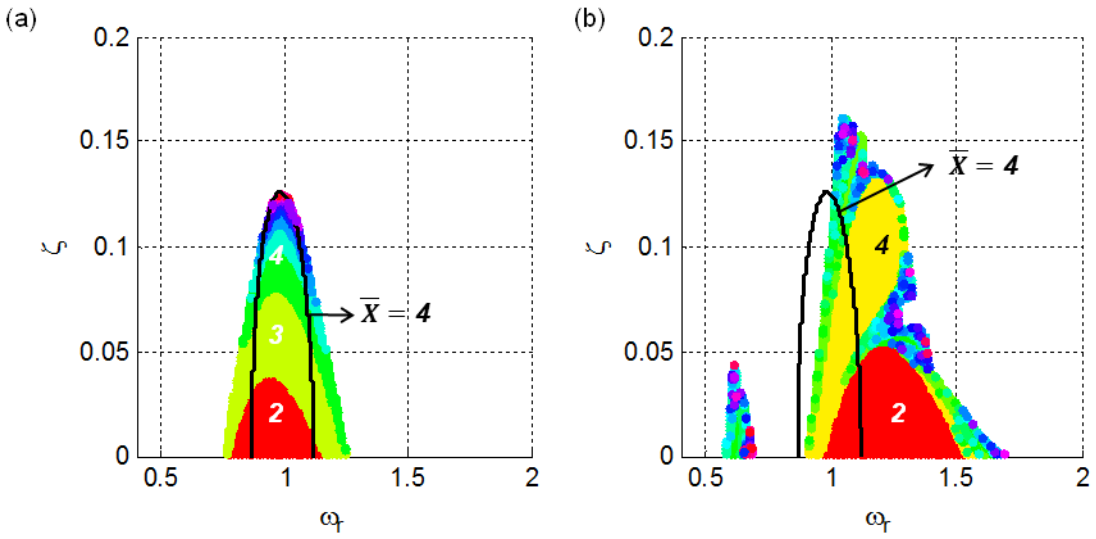

Figure 3-11. Number of zero-velocity crossings of under-actuated systems with F_r = 0.25 (a) a linear system (b) a bistable structure.

Figure 3-12 presents the number of zero-velocity crossings of the linear and the bistable systems subjected to F_r = 1. For F_r = 1, the energy function for the linear system has two main energy levels, a high energy level and a low energy level. The energy function is less quantized compared to the energy function for F_r = 0.25 and includes a wider range of excitation frequency ratio and damping ratio. For a bistable structure subjected to the same amount of force, the energy is continuous for a large domain and is quantized for large excitation frequency ratios.

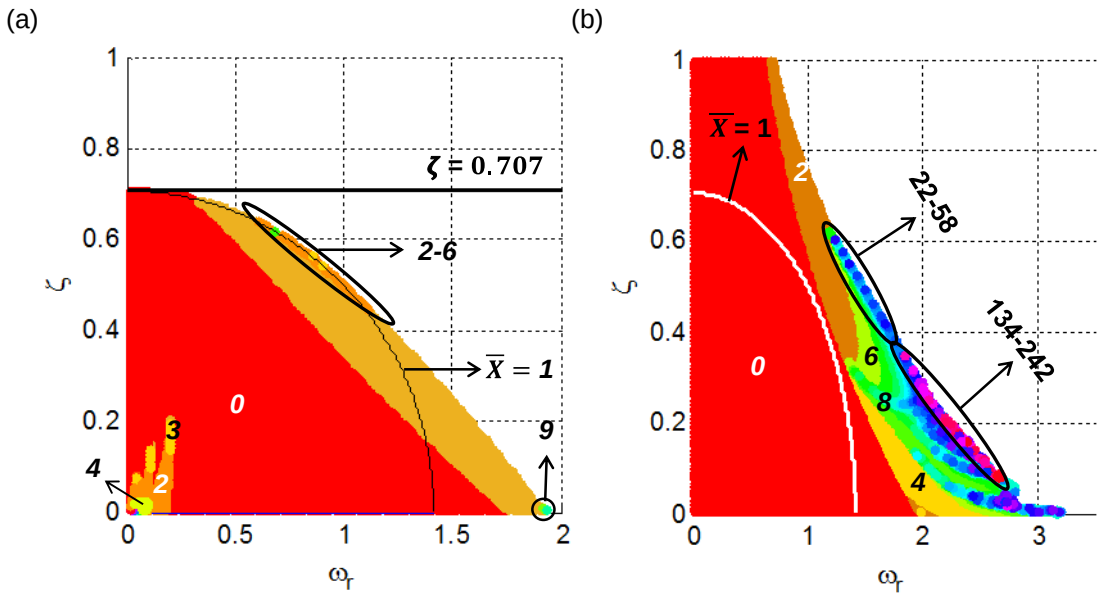

Figure 3-12. Number of zero-velocity crossings of systems with F_r = 1 (a) a linear system (b) a bistable structure.

Figure 3-13 presents the number of zero-velocity crossings of the linear and the bistable systems subjected to F_r = 1.5. The linear energy function is continuous for F_r = 1.5. For a bistable structure subjected to F_r = 1.5, energy is continuous except for a small quantized region.

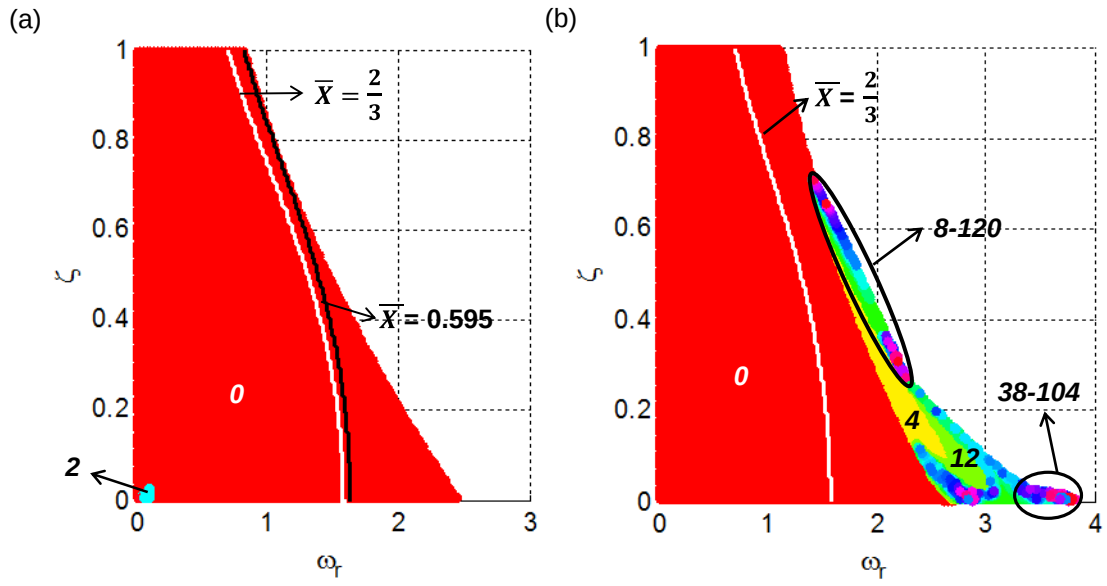

Figure 3-13. Number of zero-velocity crossings of systems with F_r = 1.5 (a) a linear system (b) a bistable structure.

Table 3-2 summarizes the ranges of frequency ratios at zero damping and damping ratio at resonant frequency capable of reaching the target displacement for the linear and the bistable systems.

Table 3-2. The ranges of damping ratio and frequency ratio, capable of reaching target displacement, for the linear and bistable systems.

F_r	ω_r at $\zeta = 0$		ζ at ω_r= 1	
	(Linear)	(Bistable)	(Linear)	(Bistable)
0.25	0.760 - 1.24	0.580 - 0.680 0.910 - 1.690	0 - 0.125	0 - 0.111
1.0	0 - 1.93	0 - 3.19	0 - 0.500	0 - 0.735
1.5	0 - 2.44	0 - 3.77	0 - 0.825	$0 < \zeta^* < \infty$

To achieve cross-well oscillation, damping ratio and excitation frequency can be selected using Table 3-2 as: $0.58 < \omega_r < 0.68$ and $0.91 < \omega_r < 1.69$ at $\zeta = 0$ and $0 < \zeta < 0.11$ at $\omega_r = 1$ for F_r = 0.25, $0 < \omega_r < 3.19$ at $\zeta = 0$ and $0 < \zeta < 0.73$ at $\omega_r = 1$ for F_r = 1, and $0 < \omega_r < 3.77$ at $\zeta = 0$ and $0 < \zeta < 1$ at $\omega_r = 1$ for F_r = 1.5. To ensure that minimum

amount of energy is spent to switch position, it is recommended to select damping ratio and excitation frequency from a narrower range as: $0.95 < \omega_r < 1.53$ at $\zeta = 0$ and $0 < \zeta < 0.053$ at $\omega_r = 1.24$ for $F_r = 0.25$, $0 < \omega_r < 2.14$ at $\zeta = 0$ and $0 < \zeta < 0.69$ at $\omega_r = 1.07$ for $F_r = 1$, and $0 < \omega_r < 2.68$ at $\zeta = 0$ and $0 < \zeta < 0.76$ at $\omega_r = 1.34$ for $F_r = 1.5$.

3.6. Conclusions

In this chapter, the energy required to actuate a bistable structure to move from one stable equilibrium position to the other in an energy and force limited scenario is investigated. To better understand the nonlinear behavior of a bistable structure, a linear system was also investigated. Both systems are excited by a single-tone harmonic force. Energy is studied as a function of damping ratio and frequency ratio for different force amplitudes because these non-dimensional parameters dictate the system response, and the system natural frequency and stable equilibrium positions do not change with the variation of the mentioned parameters.

For a linear viscously damped mechanical oscillator, it is observed that the energy function is quantized because reaching target displacement occurs during the transient region of the response, and the energy function becomes more continuous and less quantized by increasing the force amplitude. Also, applying a dynamic force (i.e. harmonic excitation) to a system makes it possible to reach displacement amplitudes that cannot be reached by applying static forces.

For a bistable structure, the required energy for cross-well oscillation is shown to vary with damping ratio and excitation frequency for different values of excitation force amplitudes. For the force amplitude less than the static force, the energy function is scattered and divided into several energy levels. By increasing the force amplitude to the static force and larger values, the ranges of excitation frequency ratios and damping

ratios able to achieve cross-well oscillation increase significantly, and the energy function becomes much more continuous.

CHAPTER 4

HARMONIC AND RANDOM EXCITATION

4.1. Introduction

The required energy for the cross-well actuation of a bistable structure, subjected to a single-tone harmonic excitation, was investigated in Chapter 3. The generated harmonic signals with the experimental devices always have some level of noise and are not purely single-tone [49]. So, it is necessary to study the required energy for performing the snap-through using a multi-tone excitation. A multi-tone signal can be created by the combination of harmonic and random signals. Iyengar [50] presented the analytical and numerical response of a Duffing-Holmes oscillator, subjected to combined harmonic and random excitation.

This chapter presents the parametric energy study for a bistable structure, subjected to a combined signal. Section 4.2 presents the design of a low-pass filter and generation of a band-limited noise. The parameter values used for energy analysis are provided in Section 4.3. Sections 4.4-4.5 provide the energy results for the linear and bistable systems. Section 4.6 presents the comparison between the energy functions for the linear and the bistable systems. Section 4.7 presents the experimental results for the multi-tone excitation of the bistable beam. Finally, Section 4.8 presents the conclusions of this chapter.

4.2. Generation of a Band-Limited Noise

A multi-tone signal is generated by combining a single-tone harmonic signal and a band-limited white noise. Band-limited white noise is generated by filtering a white

noise signal. The designed filter has cut-off and stopband frequencies of ω_c = 50 Hz and ω_s = 110 Hz, respectively. The stopband attenuation for the digital filter is 80 dB. The optimal equiripple design technique is used for this purpose since the band frequencies (ω_c and ω_s) can be specified precisely in this design. This technique is implemented in MATLAB by the Parks-McClellan algorithm as a function called *firpm* [51-53]. Figure 4-1 (a-b) show the power spectrum of white noise force signal with standard deviation (STD) of 1 N and filtered noise signal, respectively. As can be seen in Figure 4-1 (a), the white noise signal has a constant power spectral density and the signal power is the same at all frequencies. Figure 4-1 (b) represents the filtered white noise signal. The so-called colored noise signal power is the same as the white noise signal for the frequencies less than 50 Hz (the passband frequency.) The signal power starts decreasing at 50 Hz, and the power attenuation of 80 dB is observed for frequencies above 110 Hz. The passband and stopband frequencies, 50 Hz and 110 Hz, are represented with vertical red lines in Figure 4-1 (b).

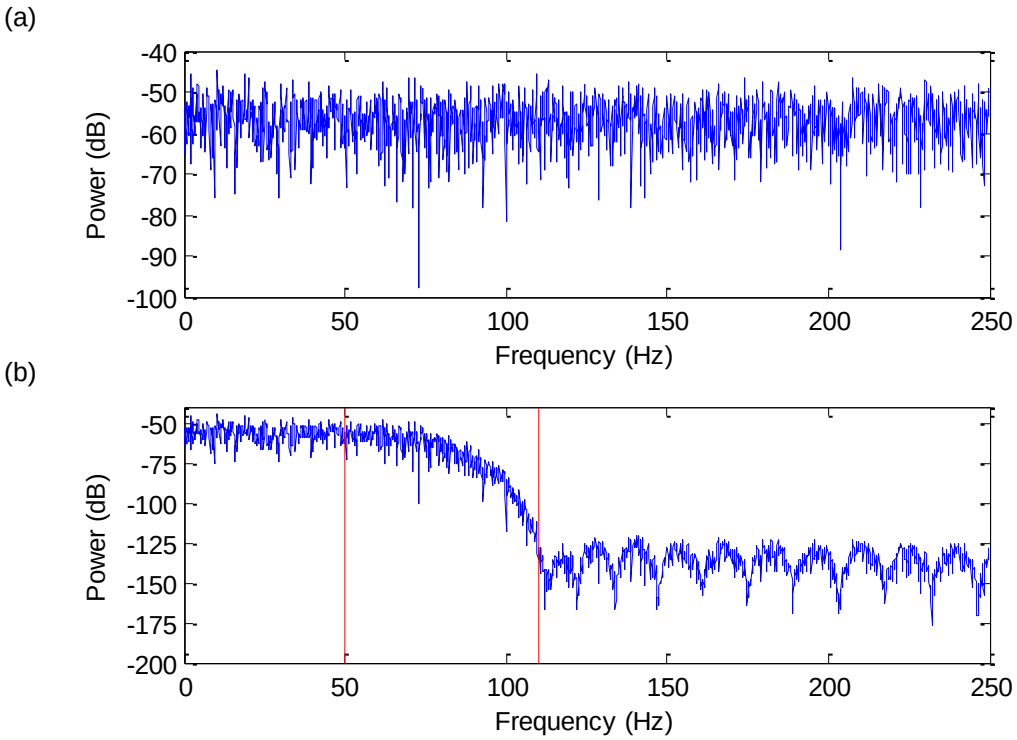

Figure 4-1. Power spectrum of: (a) white noise signal with STD of 1N (b) filtered white noise.

Figure 4-2 (a-c) present multi-tone signals with different levels of noise. The signals are the combinations of an under-actuated harmonic force with F_r= 0.25 at 13 Hz and different levels of colored noise with 50 Hz passband frequency and 110 Hz stopband frequency. The ratios of noise STD to harmonic force STD are 0.2, 0.4, and 0.8.

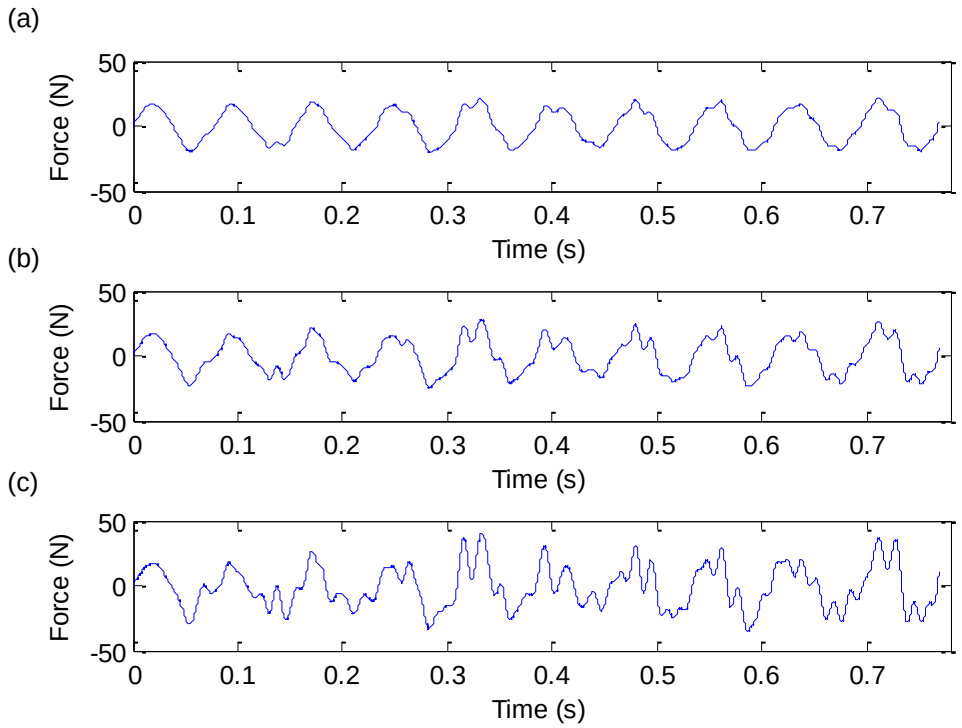

Figure 4-2. Multi-tone force with F_r = 0.25, and noise STD to harmonic STD ratio of (a) 0.2 (b) 0.4 (c) 0.8.

4.3. Experimental Results

In this section, the frequency responses of a linear beam and a bistable beam subjected to multi-tone excitations are presented. The objective is to validate the mathematical model used for the investigation of required energy for performing snap-through of a bistable structure subjected to multi-tone excitations with different levels of noise. The experimental setup is shown in Section 4.3.1. The experimental results for linear and a bistable beams are presented in Sections 4.3.2 and 4.3.3, respectively.

4.3.1. Experimental Setup

A new experimental setup, similar to that shown in Figure 2-5, is used to obtain the results in this chapter. First, the laser displacement sensor is moved from 185 mm to 105 mm from the clamped end. The charge amplifiers are replaced by a different

amplifier (PCB 482A20), but the amplification gains for the measured force and acceleration signals remain the same as before. Also, a low-pass filter device (WAVETEK 852) is added to the experimental setup. The force signal is passed through the filter before being sent to the shaker. The cut-off frequency of the filter is set to be 50 Hz. Figure 4-13 shows the experimental setup. The stable equilibrium positions are located approximately 1.13 mm below and above the unstable position at the location of the laser displacement sensor. As can be seen in the figure, the laser is located at a closer position to the base compared to the previous setup.

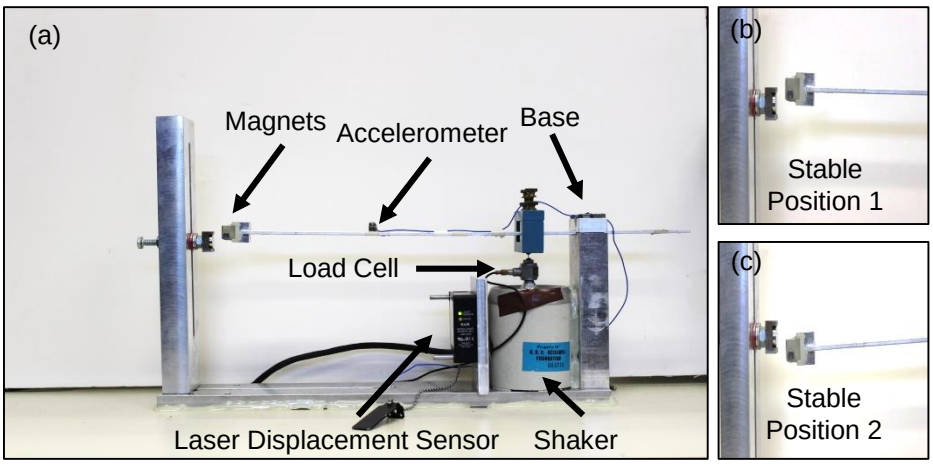

Figure 4-3. The new experimental setup: a) test apparatus, and stable equilibrium states: b) One and c) Two.

4.3.2. Linear Beam

The linear beam frequency response is measured in the 5-35 Hz frequency band to identify the linear system parameters.

Pure Noise Excitation

First, different levels of white Gaussian noise signals are generated and passed through the filter to ensure that the low-pass filter is working properly. Figure 4-4 presents the power spectra of three filtered pure noise excitation signals with STDs of

1.3 N, 2.9 N, and 5.3 N. As can be seen in the figure, the signal power starts attenuating at 50 Hz, and the attenuation continues up to the frequency of around 110 Hz.

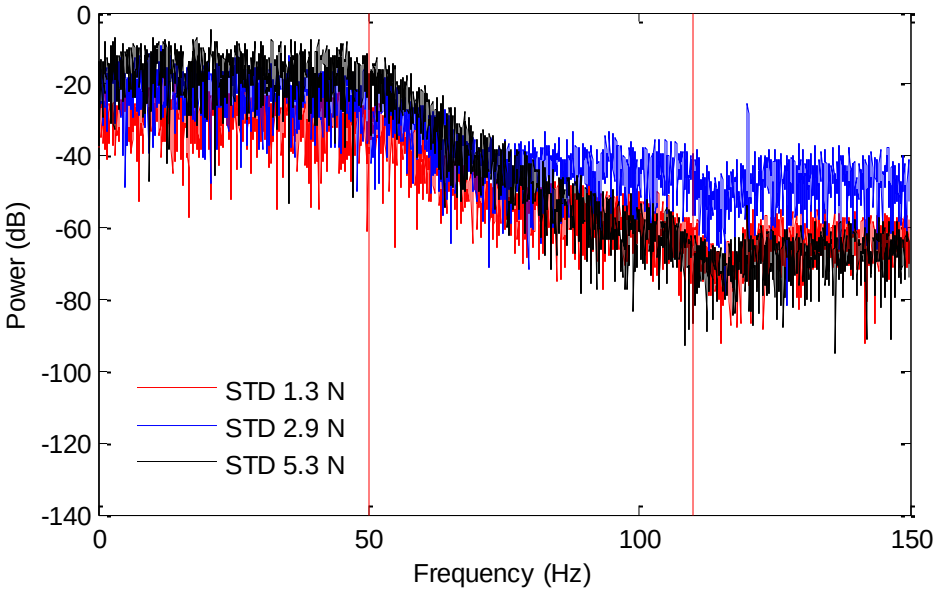

Figure 4-4. Power spectra of three filtered noises with STDs of: 1.3 N, 2.9 N, and 5.3 N.

Figure 4-5 shows the Fast Fourier Transforms (FFT) of the shown signals in Figure 4-4. The noise amplitude is very low for the frequencies above 50 Hz and gets close to zero for the frequencies above 80 Hz.

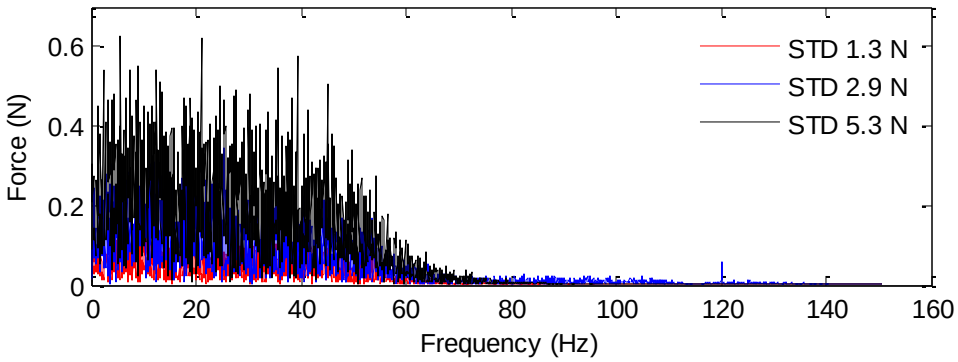

Figure 4-5. FFTs of filtered noise signal with STDs of: 1.3 N, 2.9 N, and 5.3 N.

The low-pass filter works properly and properly filters the frequency content of a signal above 50 Hz.

Multi-tone Excitation

Figure 4-6 shows the ratios of displacement to force for a linear beam subjected to multi-tone excitation having different levels of noise. The multi-tone signals have the same harmonic force amplitude of 5.6 N and are different in the level of noise. The noise standard deviations for the multi-tone signals are 1.3 N, 2.4 N, 5.3 N, and 6.7 N.

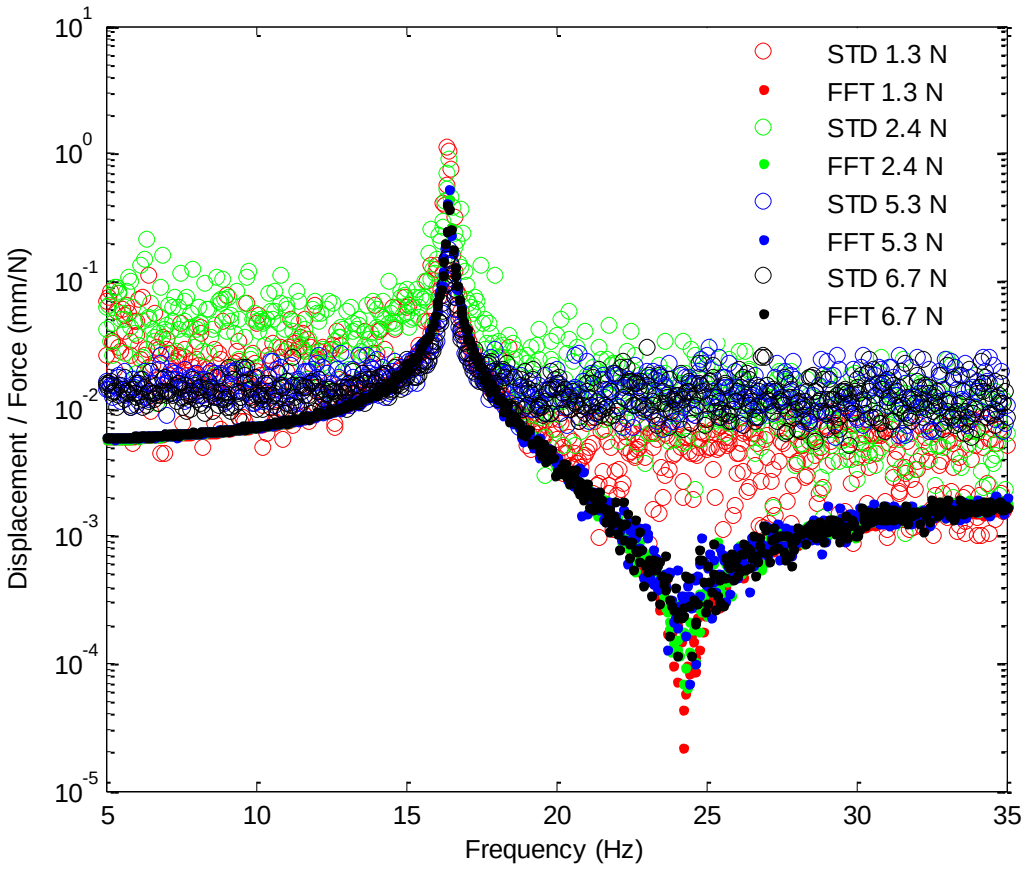

Figure 4-6. Ratios of displacement STD to force STD and displacement FFT to force FFT for multi-tone signals with noise STDs of: 1.3 N, 2.4 N, 5.3 N, and 6.7 N.

Two types of displacement to force ratios are represented in Figure 4-6. The first one is the ratio of displacement STD to force STD for different noise levels. Displacement STD and force STD are obtained by finding the STD of recorded time histories of force and displacement signals at each frequency. The second metric is the ratio of displacement FFT peak value to force FFT peak value. First, the FFTs of excitation force and displacement signals are found at each frequency. Then the maximum values for force and displacement within 0.5 Hz above and below that frequency in the frequency domain are deduced. These values represent the amplitude of the harmonic components of multi-tone signals. Figure 4-7 presents the ratio of displacement to force for multi-tone excitation with different harmonic amplitudes and

the same level of noise with STD of 1.3 N. In Figure 4-7, F_0 shows the amplitude of the harmonic component.

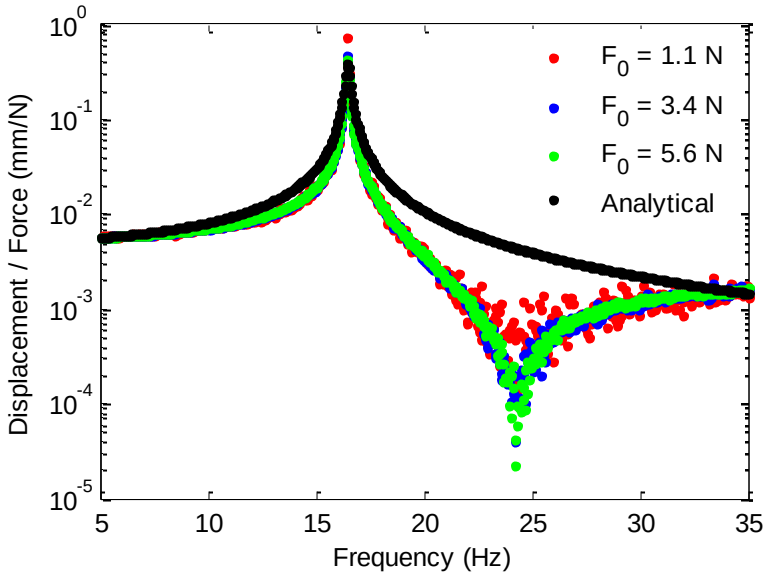

Figure 4-7. Experimental ratios of displacement FFT to force FFT for the multi-tone signal with harmonic amplitude of 1.1 N, 3.4 N and, 5.6 N and same noise STD of 1.3 N and analytical identified displacement to force ratio.

The identified parameters for the linear beam are shown in Table 4-1. Two sets of identified parameters are presented in the table: linear system 1 and linear system 2. The linear system 1 column demonstrates the identified parameters for the linear beam used in Chapter 2, and the parameters in the linear system 2 column describe the identified parameters for the linear beam used in Chapter 4.

Table 4-1. The identified parameters for linear beams used in Chapter 2 and Chapter 4.

Parameter	Linear System 1	Linear System 2
m (kg)	16.5	16.6
k_1 (N/m)	$1.77*10^5$	$1.78*10^5$
k_3 (N/m)	0	0
ζ	0.006	0.006

The identified parameters shown in Table 4-1 are very close since the same beam is used in Chapter 2 and Chapter 4, and only the laser displacement sensor is moved to a closer location to the base for the experiments in Chapter 4. Also, it should be noted that F_{static} = 60 N for the experimental bistable beam. Static force is calculated as the product of linear stiffness, location of stable position, and a geometric correction factor of 0.29.

4.3.3. Bistable Beam

In this section, the experimental results for the cantilevered bistable beam are presented.

Harmonic Force Amplitude of 1.1 N (F_r= 0.02)

In this section, the frequency response of the bistable to excitations with low harmonic amplitude of 1.1 N is presented. The bistable beam shows linear behavior at low excitation amplitudes since it oscillates around one potential well. The numerical and experimental frequency responses for the bistable beam subjected to the pure harmonic excitation of amplitude 1.1 N are presented in Figure 4-8. The identified linear stiffness for the beam in this chapter multiplied by a correction factor of 0.78 is used for the numerical calculation of frequency response at harmonic amplitude of 1.1 N. Damping ratio is also increased to 0.008 for finding theoretical displacement to force ratio.

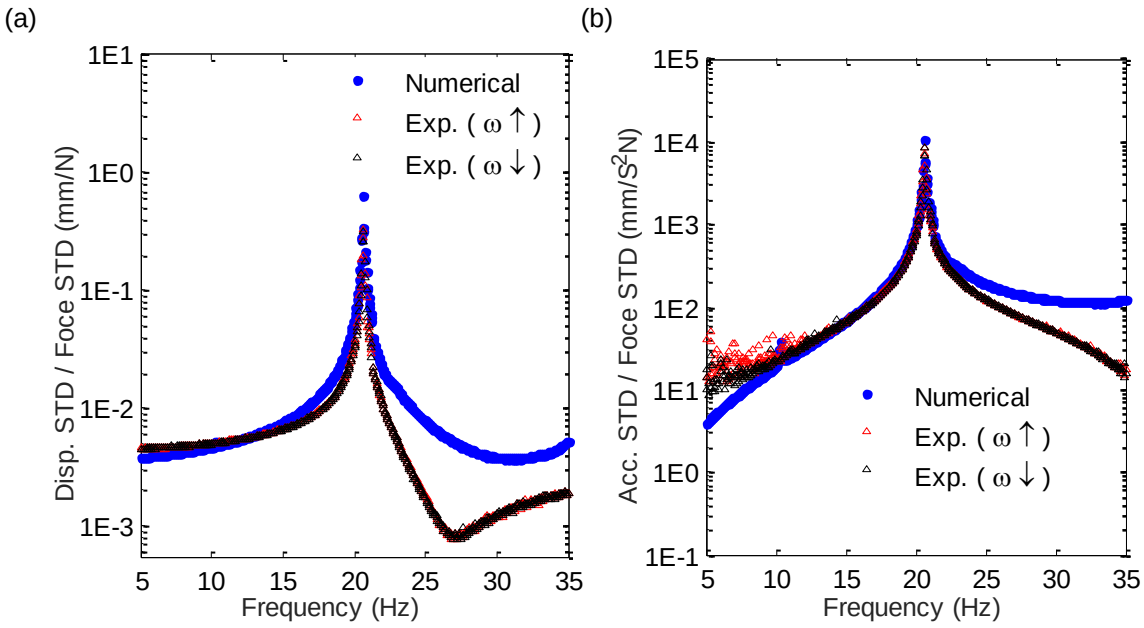

Figure 4-8. Numerical and experimental frequency responses of the bistable beam subjected to harmonic excitation with the amplitude of 1.1 N: (a) displacement STD to force STD (b) acceleration STD to force STD.

As can be seen in Figure 4-8, the bistable beam behaves like a linear system for low excitation forces, and the acceleration and displacement frequency responses have sharp narrow peaks near the resonance frequency. There is an acceptable match between numerical and experimental results for frequencies less than 22 Hz. As expected, the difference between numerical and experimental results is higher at post-resonance frequencies. This is mainly because the effect of higher modes of vibration is dominant at high frequencies, and the mathematical model is only able to predict the single-mode behavior of the bistable structure. The numerical and experimental displacement bifurcation diagrams are represented in Figure 4-9. The numerical and experimental bifurcation diagrams look the same except at the resonant frequency. It seems that a jump in displacement exists at resonance for the numerical bifurcation diagram. Overall, both bifurcation diagrams predict the same dynamical behavior for the bistable system.

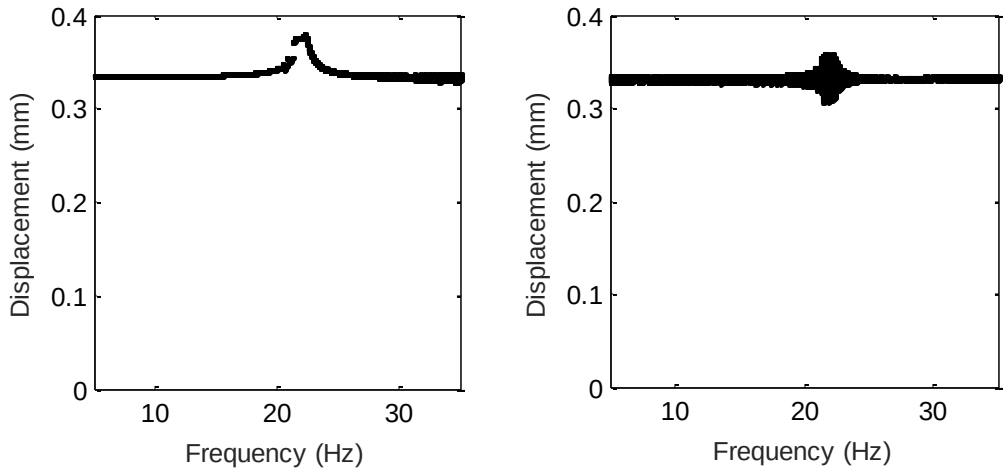

Figure 4-9. Displacement bifurcation diagrams for 1.1 N harmonic force amplitude: (a) numerical (b) experimental.

Figure 4-10 shows the frequency responses of the bistable beam subjected to excitation with different levels of noise. All of the excitations have the same harmonic amplitude of 1.1 N. The frequency response has a sharp resonance peak for pure harmonic excitation. The resonance peak decreases by adding noise with 1.3 N STD to the harmonic input. By increasing noise STD to 2.4 N, the peak flattens out and the displacement to force ratio looks like a flat line in the entire frequency band. With an increase of noise STD to 5.3 N, the frequency response magnitude increases, and it gets scattered in the entire range.

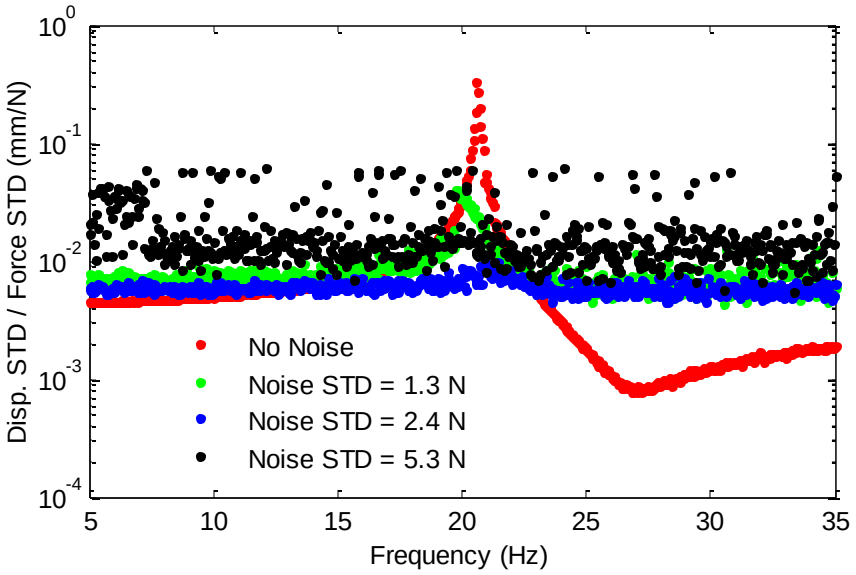

Figure 4-10. Experimental ratios of displacement STD to force STD for the excitation with harmonic amplitude of 1.1 N and noise STD of 0 N, 1.3 N, 2.4 N, and 5.3 N.

Figure 4-11 presents the experimental mean displacement for excitation with harmonic amplitude of 1.1 N and different levels of noise. In Figure 4-11, X_{01} and X_{02} are the locations of positive and negative stable equilibrium positions, respectively. For pure harmonic excitation and excitations with noise STDs of 1.3 N and 2.4 N, the bistable system has a single-well oscillation since the displacement mean is very close to the positive potential well in the entire frequency range. For the highest level of noise, the bistable system is achieving snap-through at various frequencies. The displacement mean is close to zero when the system is moving back and forth between negative and positive potential wells. It is observed that high levels of noise can induce snap-through in a bistable structure, even for low-amplitude harmonic excitations.

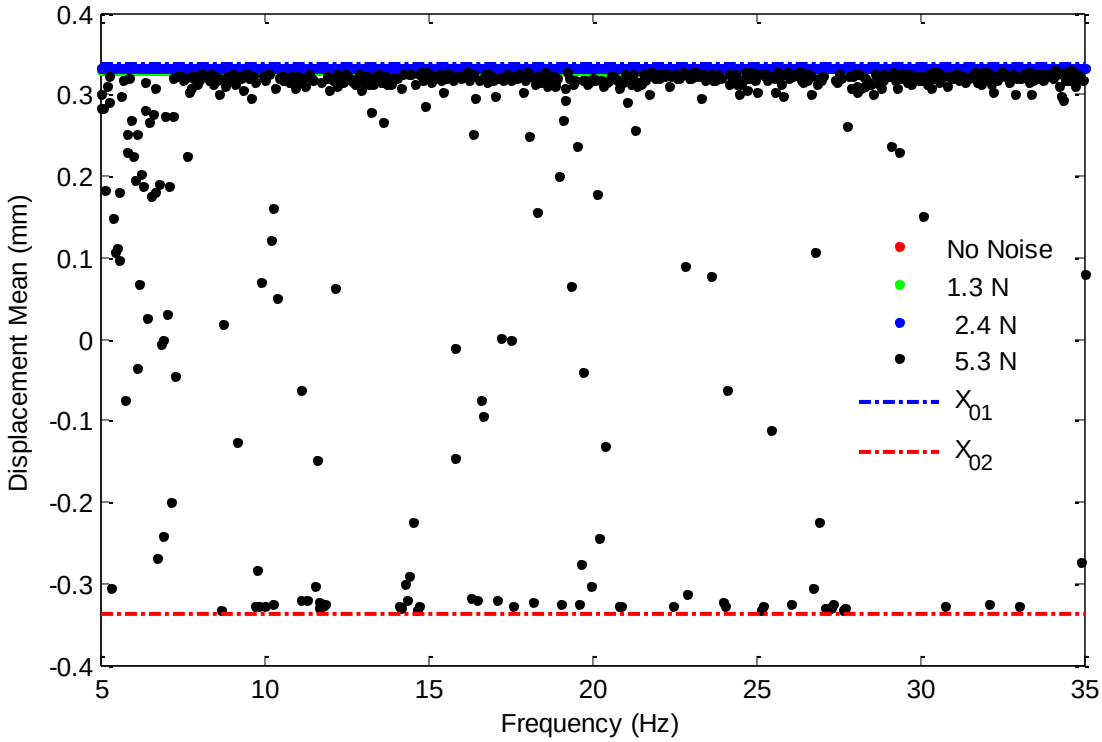

Figure 4-11. Experimental mean displacement for excitation with harmonic amplitude of 1.1 N and noise STD of 0 N, 1.3 N, 2.4 N, and 5.3 N.

Harmonic Force Amplitude of 15.5 N (F_r= 0.26)

The bistable beam is excited with large harmonic force amplitudes to ensure that the response shows nonlinear behavior. Figure 4-12 presents displacement for excitation with harmonic amplitude of 15.5 N and different noise levels. Jumps exist in displacement for all excitations. For noise STD of 2.4 N, the beam is achieving single-well oscillation around the positive potential well. For pure harmonic excitation and noise STD of 1.3 N, the beam is achieving oscillation around the top stable position up to the frequency of around 17.8 Hz. Then, the beam is snapping from the top stable position to the bottom one at around 17.8 Hz and continues oscillating around the bottom stable position for these two excitations. Also, the beam is achieving cross-well motion at 17.8 Hz for noise STD of 1.3 N. For the highest noise level, the bistable beam is able to perform snap-through in the entire frequency domain.

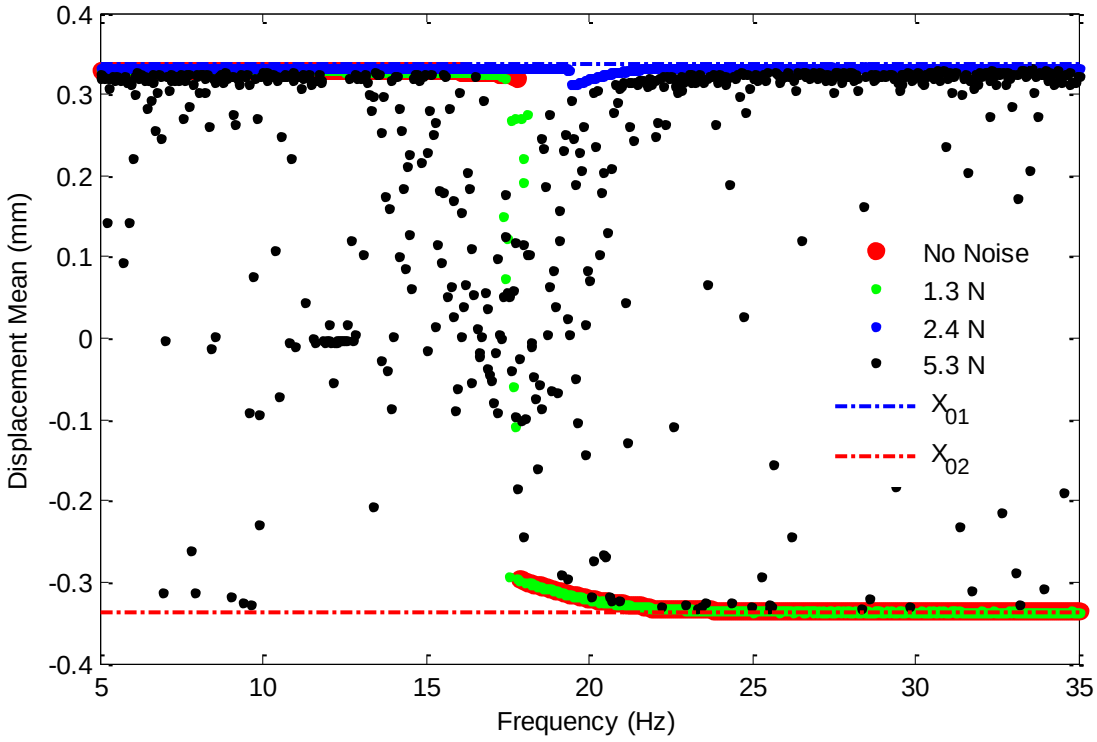

Figure 4-12. Experimental mean displacement for the excitation with harmonic amplitude of 15.5 N and noise STD of 0 N, 1.3 N, 2.4 N, and 5.3 N.

4.4. Parametric Analysis

The parameters used for studying the required energy for cross-well actuation of the bistable structure subjected to multi-tone excitation are the same as the ones used in Chapter 3 for single-tone harmonic excitation. Three different force amplitudes are considered: one quarter of the static force, equivalent to the static force, and 1.5 times the static force. Energy functions are plotted for four different ratios of noise STD to harmonic STD for an under-actuated bistable system. F_n is defined as the ratio of noise STD to harmonic STD. F_n values are: 0.2, 0.4, and 1.

Table 4-2. Parameters for numerical simulations.

Parameter	Range
m (kg)	1.00
ω_n (Hz)	13.0
ζ	0 - 1
k_1 (N/m)	ω_n^2
Δ	$1.00*10^4$
k_3 (N/m)	$6.67*10^3$
$F_r = F_0/F_{static}$	0.250
F_n	0.20, 0.40, 1.0
$\omega_r = \omega/\omega_n$	0 - 8

The energy functions for the linear and the bistable systems are presented in the following sections for different harmonic force amplitudes and levels of noise.

4.5. Linear System Energy Behavior

Figure 4-13 represents the energy function for an under-actuated linear system subjected to excitation with different levels of noise. The energy function for pure harmonic excitation is shown in Figure 4-13 (a). By adding the colored noise signal to harmonic excitation in Figure 4-13 (b), the linear system is able to reach the objective position for low excitation frequencies and low damping ratios. Also, several high energy points can also be seen around the excitation frequency equal to the natural frequency and high damping ratios. Further, by increasing F_n to 0.4 in Figure 4-13 (c), the linear system is able to reach the target displacement at higher excitation frequencies and low damping ratios. For the highest level of noise (F_n = 1) in Figure 4-13 (d), the range of damping ratio shows significant increase. As can be observed in this figure, there are many points at higher damping ratios in the whole excitation frequency range capable of reaching the target displacement.

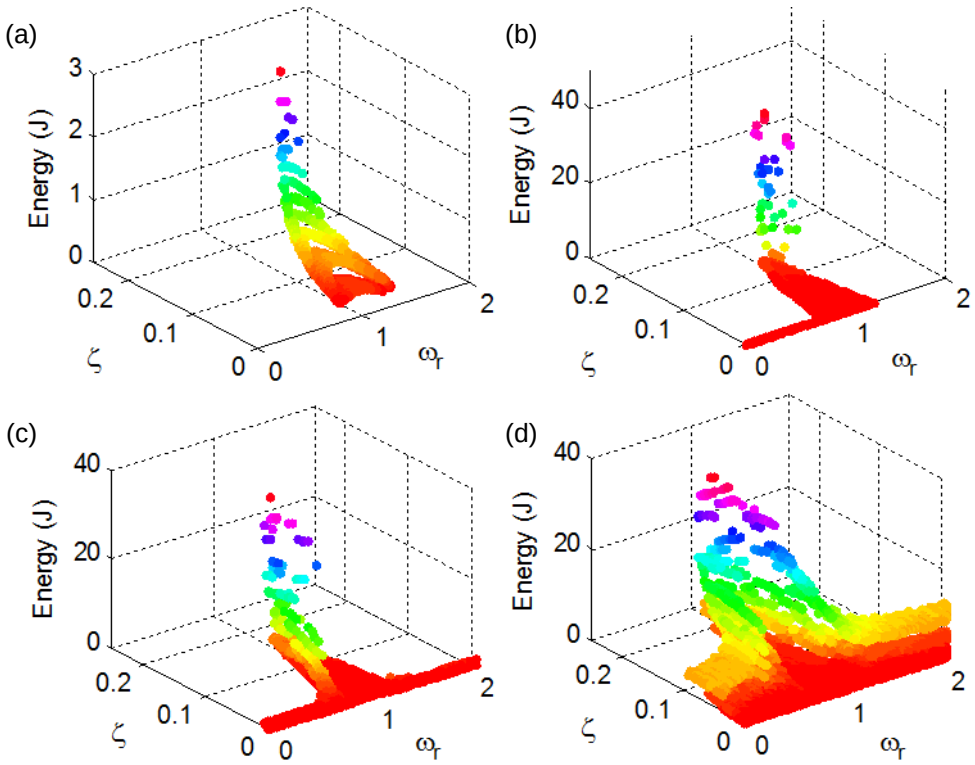

Figure 4-13. Total energy of a linear system with F_r = 0.25 as a function of frequency ratio and damping ratio for (a) pure harmonic excitation and excitation with F_n of (b) 0.2 (c) 0.4 (d) 1.

Figure 4-14 shows the normalized damping energy functions for an under-actuated linear system. The normalized damping energy is the ratio of damping energy to the total energy. As can be seen in Figure 4-14, the range of excitation frequency ratio reaches up to eight for cross-well transfer by increasing the level of noise. Also, the linear system can reach the objective displacement at excitation frequencies close to zero. The color in Figure 4-14 is proportional to the number of zero-velocity crossings at each point, and the color bar presents the color distribution for the shown range of number of zero-velocity crossings. Also, the color is proportional to the number of zero-velocity crossings for all normalized damping energy functions in the preceding pages.

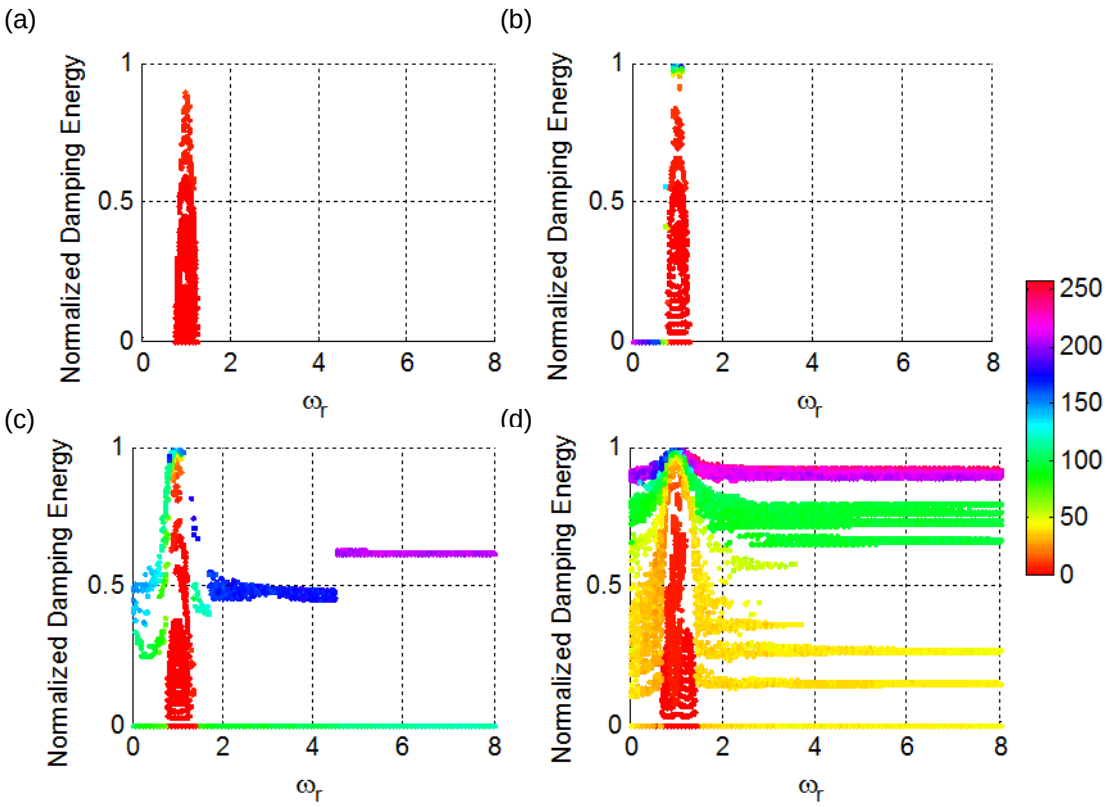

Figure 4-14. Normalized damping energy of a linear system with F_r = 0.25 as a function of frequency ratio and damping ratio for (a) pure harmonic excitation and excitation with F_n of (b) 0.2 (c) 0.4 (d) 1.

Figure 4-15 shows the normalized damping energy functions. The range of damping ratio changes from 0.13 to 0.25 by increasing F_n from 0 to 1. Additionally, the number of points for the highest level of noise in Figure 4-15 (d) is much larger compared to the energy functions with lower levels of noise in Figure 4-15 (a-c).

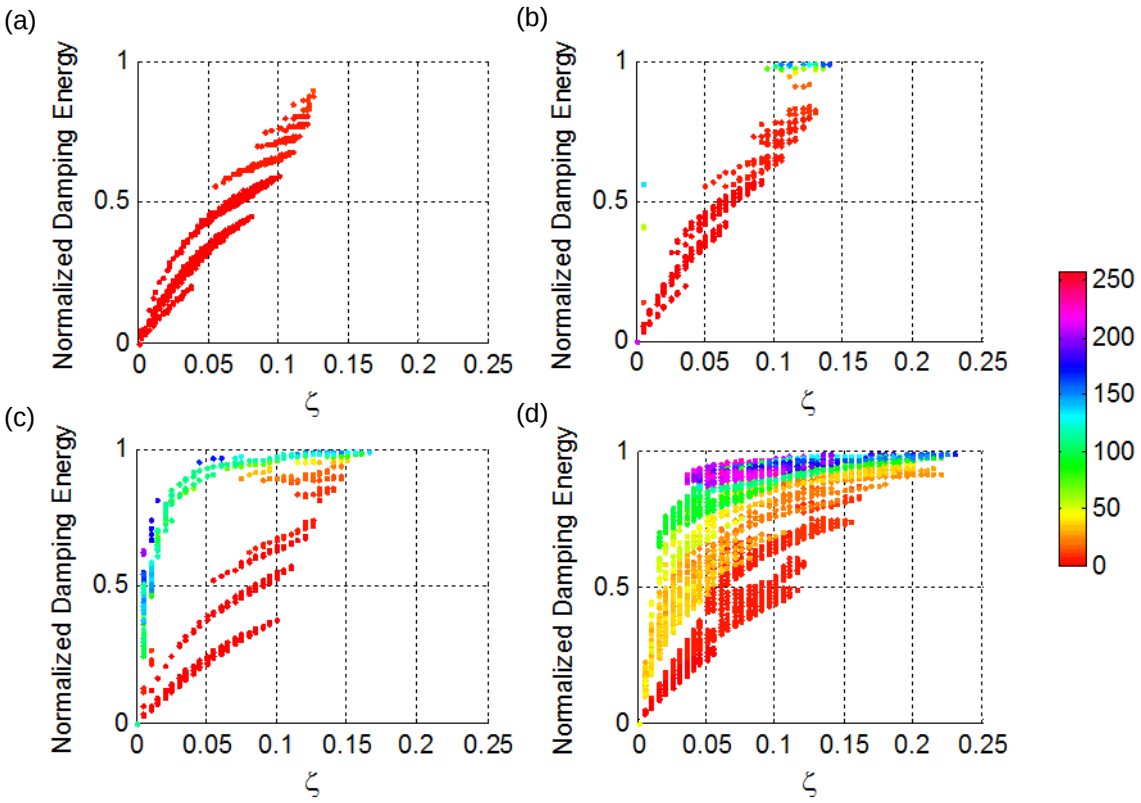

Figure 4-15. Normalized damping energy of a linear system with F_r = 0.25 as a function of frequency ratio and damping ratio for (a) pure harmonic excitation and excitation with F_n of (b) 0.2 (c) 0.4 (d) 1.

4.6. Bistable System Energy Behavior

This section presents the energy functions for an under-actuated bistable structure. Figure 4-16 shows the energy functions for the excitations with different levels of noise. As can be seen in Figure 4-16 (a), the bistable system is not capable of achieving cross-well oscillation at low excitation frequencies for pure harmonic excitation. As can be seen in Figure 4-16 (b), the bistable system achieves cross-well oscillation at excitation frequencies close to zero and at high excitation frequencies by adding noise to the harmonic input. Furthermore, by increasing the noise content of the signal, the range of excitation frequency and damping ratio increase, and the bistable system, as shown in Figure 4-16 (d), is able to perform snap-through at low frequencies and high damping ratios.

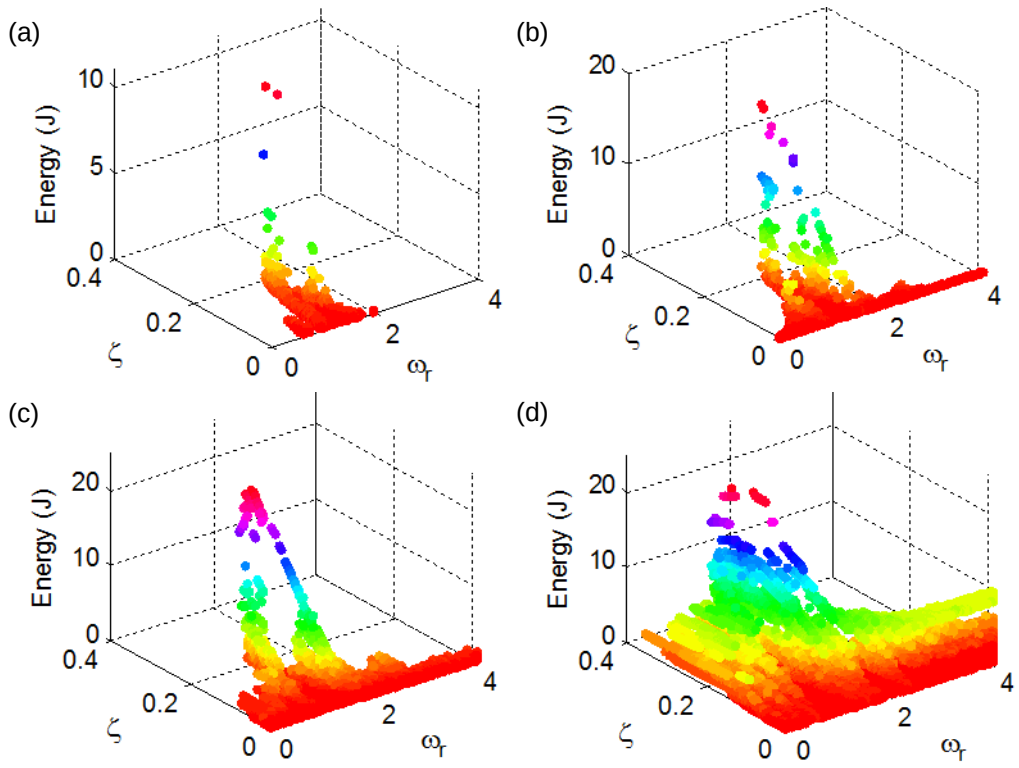

Figure 4-16. Total energy of a bistable structure with F_r = 0.25 as a function of frequency ratio and damping ratio for (a) pure harmonic excitation and excitation with F_n of (b) 0.2 (c) 0.4 (d) 1.

Figure 4-17 shows the normalized damping energy functions for an under-actuated bistable system. The maximum normalized damping energy in Figure 4-17 is around 50% for the pure harmonic excitation. By adding noise to the harmonic signal, the normalized damping energy increases and reaches up to 99%, as shown in Figure 4-17 (b-d). Also, the maximum excitation frequency ratio increases from two for pure harmonic input to eight for the bistable systems subjected to excitations with non-zero noise content.

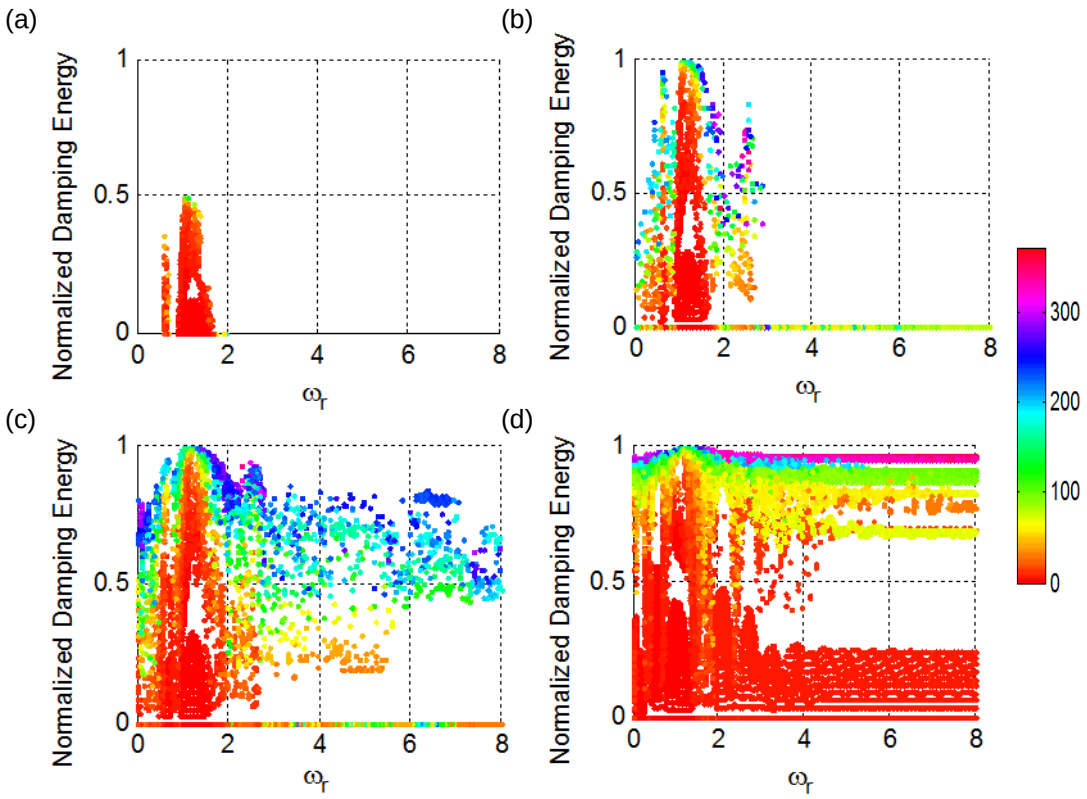

Figure 4-17. Normalized damping energy of a bistable structure with F_r = 0.25 as a function of frequency ratio and damping ratio for (a) pure harmonic excitation and excitation with F_n of (b) 0.2 (c) 0.4 (d) 1.

Figure 4-18 shows the normalized damping energy form. The mentioned findings can also be observed in this figure. Specifically, the maximum damping ratio is less than 0.17 for the pure harmonic excitation. This value goes up to around 0.37 for the maximum noise level considered here.

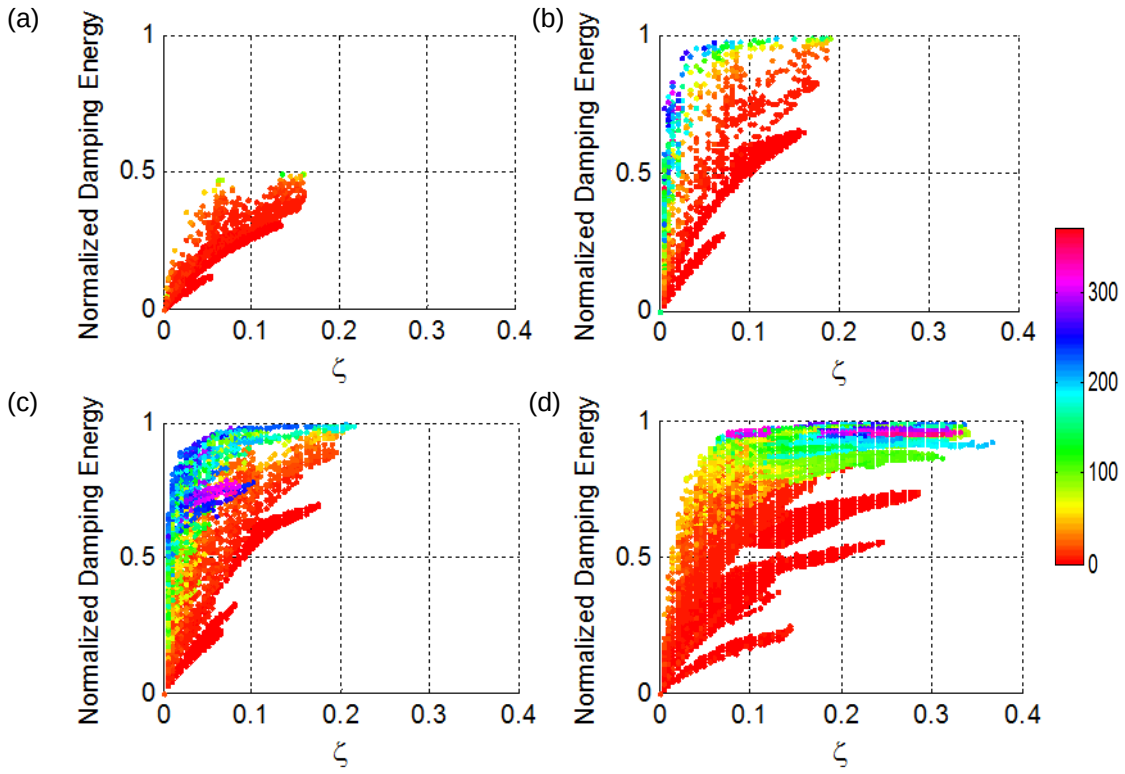

Figure 4-18. Normalized damping energy of a bistable structure with F_r = 0.25 as a function of frequency ratio and damping ratio for (a) pure harmonic excitation and excitation with F_n of (b) 0.2 (c) 0.4 (d) 1.

4.7. Comparison of Linear and Bistable Systems

In this section, the energy functions for the linear and the bistable systems are compared. Figure 4-19 shows the comparison between the total energy functions. The linear and bistable energy functions are placed in the right and left columns, respectively. The bistable system has larger ranges of damping ratio and excitation frequency for all excitations. In addition, the energy functions for both the bistable and the linear systems look very similar for the highest level of noise in Figure 4-19 (g-h). As expected, it is shown that the linear and bistable systems behave similarly under a high level of noise.

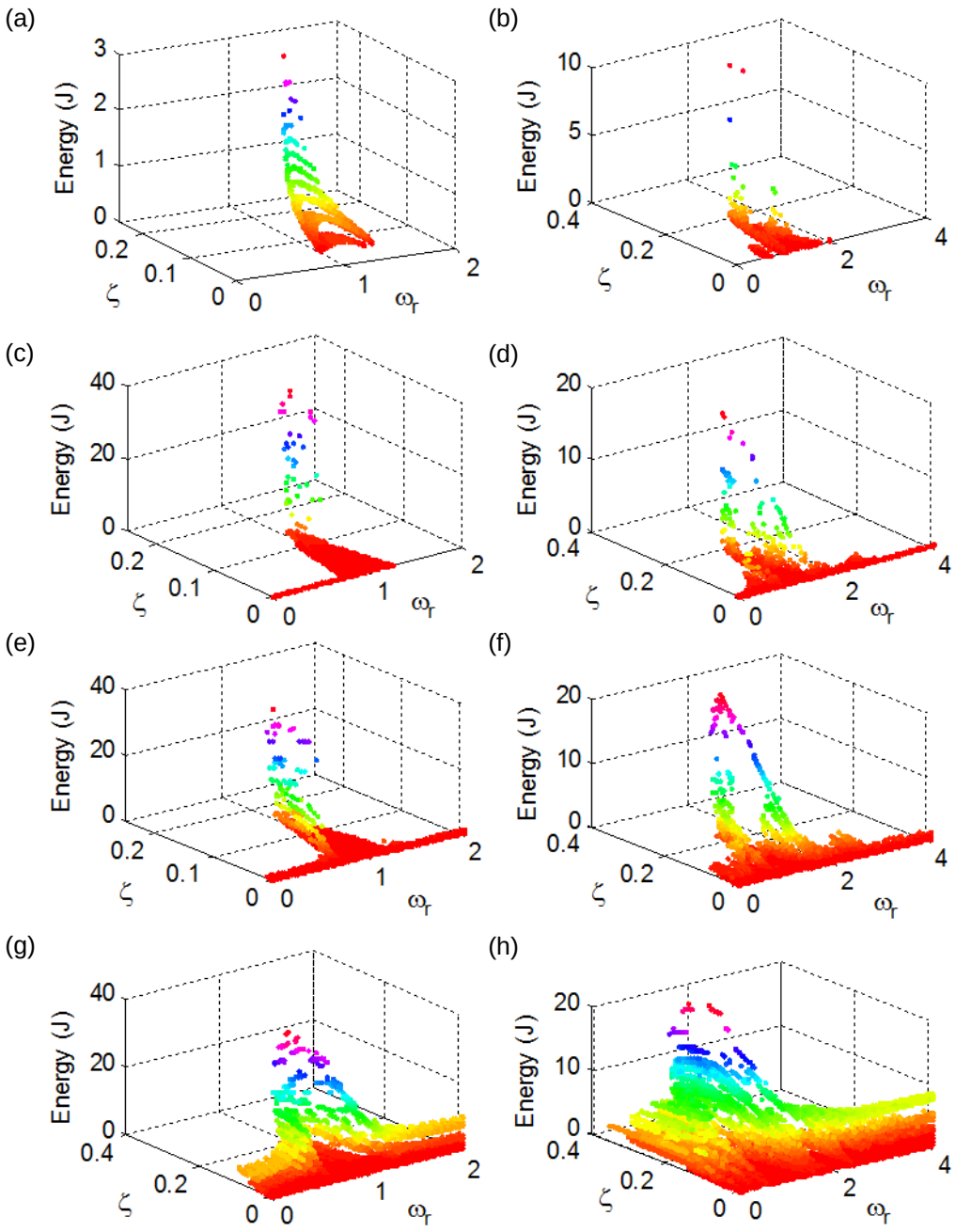

Figure 4-19. Comparison between total energies of a linear system (left column) and a bistable system (right column) subjected to: (a-b) pure harmonic excitation and excitations with F_n of: (c-d) 0.2 (e-f) 0.4 (g-h) 1.

Figure 4-20 presents the comparison between normalized damping energy functions. For pure harmonic excitation, the maximum damping energies are around 98% and 50% for linear and bistable systems, respectively.

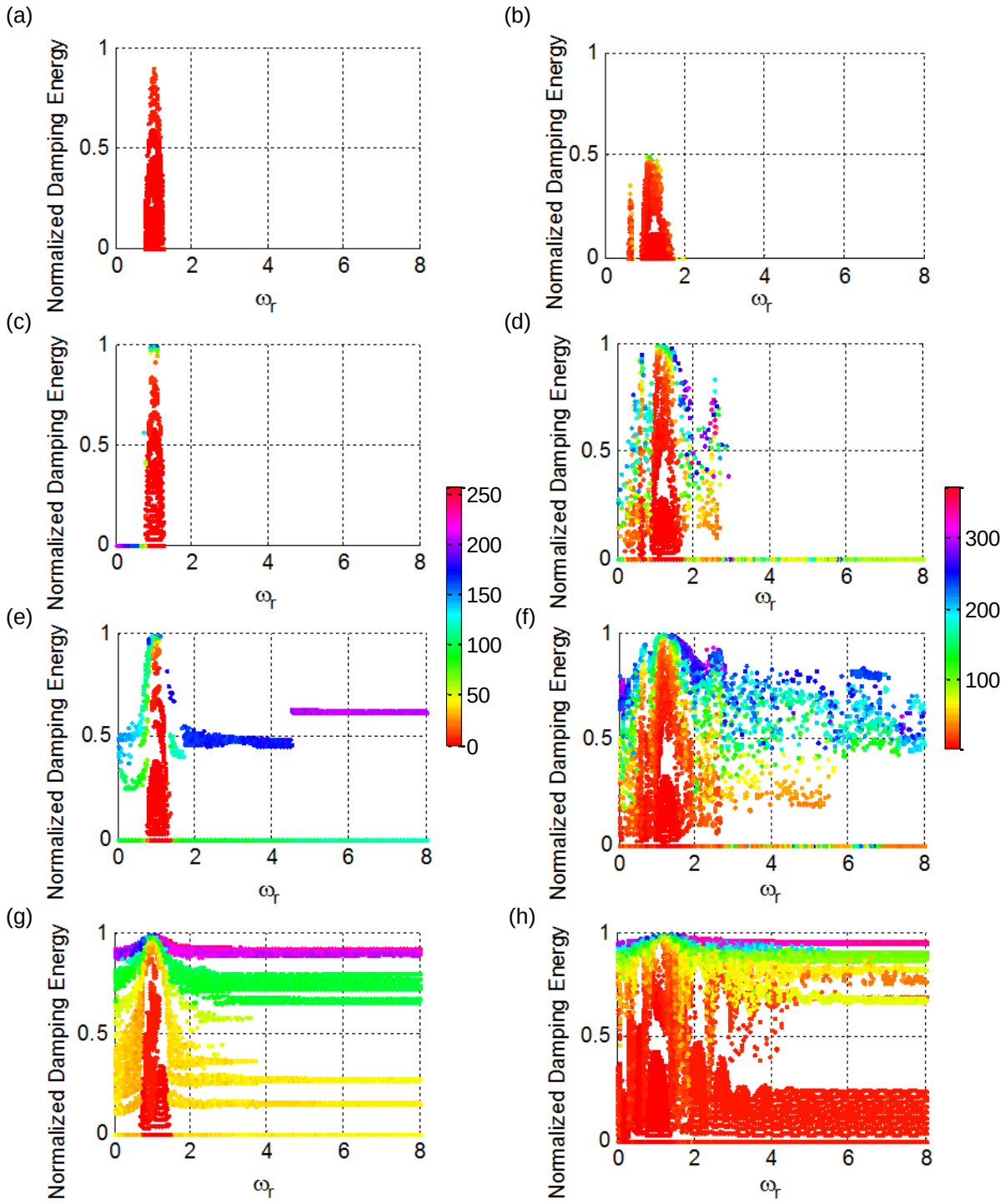

Figure 4-20. Comparison between damping energies of a linear system (left column) and a bistable system (right column) subjected to: (a-b) pure harmonic excitation and excitations with $F_n$of: (c-d) 0.2 (e-f) 0.4 (g-h) 1.

Figure 4-21 presents the comparison between normalized damping energy functions. The energy functions look very similar for the largest level of noise.

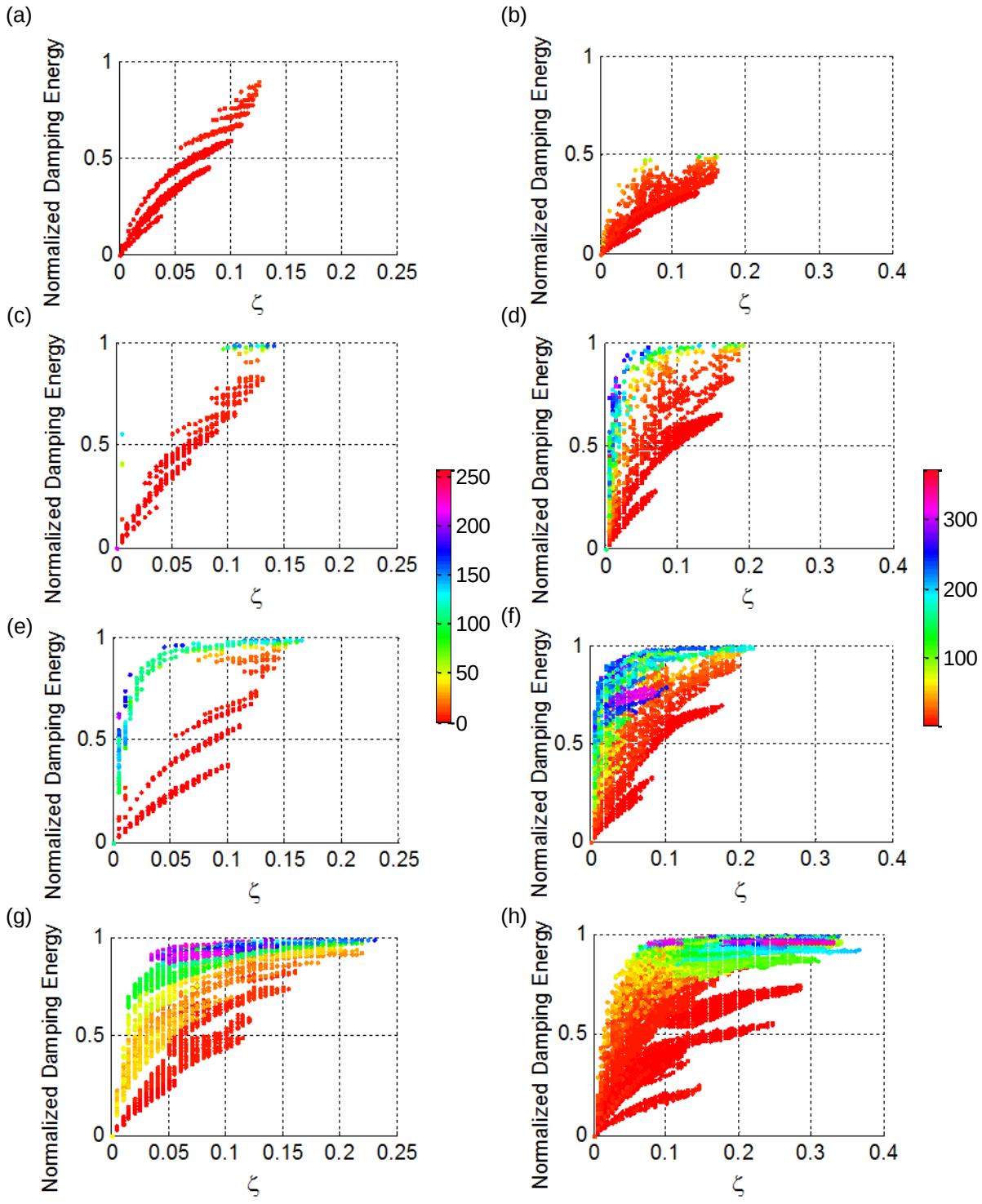

Figure 4-21. Comparison between damping energies of a linear system (left column) and a bistable system (right column) subjected to: (a-b) pure harmonic excitation and excitations with F_n of: (c-d) 0.2 (e-f) 0.4 (g-h) 1.

4.8. Conclusions

In this chapter, the energy required to perform a snap-through in a bistable structure subjected to a band-limited noise input is studied. To better understand the bistable system energy function, the required energy is also studied for a linear system.

The range of damping ratio and excitation frequency in the linear and bistable energy functions increase by increasing the level of noise. It is observed that a bistable system has a larger range of excitation frequency and damping ratio compared to a linear system for the same force input. Additionally, the bistable and linear system energy functions look very similar for high levels of noise.

CHAPTER 5

CONCLUSIONS AND FUTURE WORK

This research investigated the minimum required energy for performing snap-through of a bistable structure. Energy is studied as a function of excitation frequency and damping ratio for different values of excitation force amplitudes and different noise levels.

The well-known one-degree-of-freedom Duffing-Holmes equation is used to mathematically model a bistable structure. The mathematical model is validated by building and testing a magneto-elastic beam subjected to harmonic excitation.

The required energy is calculated by solving the Duffing-Holmes equation subjected to single-tone harmonic and multi-tone excitations.

First, this chapter summarizes the results of this research. Next, papers published based on this research are listed. Finally, future recommendations are made.

5.1. Summary of Results

Chapter 2 discusses the mathematical modeling of a bistable structure using a one-degree-of-freedom Duffing-Holmes oscillator and the experimental validation of the model. A cantilevered bistable beam was fabricated for the experiments. There is a good match between predicted analytical results and experimental frequency responses. A number of important issues exist that are responsible for the discrepancy between experimental and numerical results. First, a mathematical model with symmetric potential wells is used to model the experimental response. Second, a one-degree-of-freedom model was used for the bistable beam by making an assumption that the bistable beam is vibrating in its first mode of bending. The single-mode vibration

assumption creates differences between numerical and experimental results at high frequencies when the bistable beam has other modes of vibration in addition to the first bending mode.

Chapter 3 demonstrated an understanding of the required energy for cross-well oscillation as a function of damping ratio and excitation frequency for different values of excitation force amplitudes. To better understand the nonlinear behavior of a bistable structure, a linear system is also investigated. Both systems are excited by a single-tone harmonic force. For a linear, viscously damped mechanical oscillator, it is observed that the energy function is quantized because reaching target displacement occurs during the transient region of the response, and the energy function becomes more continuous and less quantized by increasing the force amplitude. The energy function of a bistable structure is scattered and divided into several energy levels for the force amplitude less than the static force. By increasing the force amplitude to the static force and larger values, the ranges of excitation frequency ratios and damping ratios able to achieve cross-well oscillation increase significantly, and energy function becomes much more continuous.

Chapter 4 extends the energy investigation of the bistable structure subjected to a band-limited noise input. To better understand the bistable system energy function, the required energy is also studied for a linear system. The range of damping ratio and excitation frequency in the linear and bistable energy functions increase by increasing the level of noise. It is observed that a bistable system has a larger range of excitation frequency and damping ratio compared to a linear system for the same force input. Additionally, the bistable and linear energy functions look very similar for high levels of noise. There is an acceptable match between the theoretical results and the experimental results.

5.2. Related Publications

In the development of this dissertation, a paper was presented at a conference. Another paper was published in the AIAA Journal. These papers are referenced below.

1. M. Zarepoor and O. Bilgen, "Constrained-Energy Cross-Well Actuation of the Duffing-Holmes Oscillator", 57th AIAA/ASCE/AHS/ASC Structures, Structural Dynamics, and Materials Conference, AIAA SciTech, (AIAA 2016-0201).
2. M. Zarepoor and O. Bilgen, "Constrained-Energy Cross-Well Actuation of Bistable Structures," AIAA Journal, pp. 1-4, 2016, http://dx.doi.org/10.2514/1.J055148.
3. Rebecca Hattery, Masoud Zarepoor, Onur Bilgen, "A Review of Modeling of Piezocomposite Structures", In Review.

5.3. Future Research

A point load is used to actuate the linear system and the bistable system in this dissertation. Future research can focus on distributed actuation of a bistable structure by using piezoelectric actuators. Further, the effect of hysteresis on the required energy for piezoelectric cross-well actuation of bistable structures can be investigated.

REFERENCES

[1] A. Arrieta, O. Bilgen, M. Friswell, and P. Hagedorn, "Passive load alleviation bi-stable morphing concept," *AIP Advances,* vol. 2, p. 032118, 2012.

[2] O. Bilgen, A. F. Arrieta, M. I. Friswell, and P. Hagedorn, "Dynamic control of a bistable wing under aerodynamic loading," *Smart Materials and Structures,* vol. 22, p. 025020, 2013.

[3] W. G. Cady, *Piezoelectricity: An introduction to the theory and application of electromechanical phenomena in crystals*: McGraw-Hill, 1946.

[4] "IEEE Standard on Piezoelectricity," *ANSI/IEEE Std 176-1987,* p. 0_1, 1988.

[5] D. J. Leo, *Engineering analysis of smart material systems*: John Wiley & Sons, 2007.

[6] E. Carrera, G. Giunta, and M. Petrolo, *Beam structures: classical and advanced theories*: John Wiley & Sons, 2011.

[7] S. M. Han, H. Benaroya, and T. Wei, "Dynamics of transversely vibrating beams using four engineering theories," *Journal of sound and vibration,* vol. 225, pp. 935-988, 1999.

[8] Wikipedia. (2016, March). *Timoshenko beam theory*. Available: https://en.wikipedia.org/wiki/Timoshenko_beam_theory#/media/File:TimoshenkoBeam.svg

[9] H. Matoba, T. Ishikawa, C. J. Kim, and R. S. Muller, "A bistable snapping microactuator," in *Micro Electro Mechanical Systems, 1994, MEMS'94, Proceedings, IEEE Workshop on*, 1994, pp. 45-50.

[10] M. Hoffmann, P. Kopka, and E. Voges, "All-silicon bistable micromechanical fiber switch based on advanced bulk micromachining," *Selected Topics in Quantum Electronics, IEEE Journal of,* vol. 5, pp. 46-51, 1999.

[11] J. Casals-Terre, A. Fargas-Marques, and A. M. Shkel, "Snap-action bistable micromechanisms actuated by nonlinear resonance," *Microelectromechanical Systems, Journal of,* vol. 17, pp. 1082-1093, 2008.

[12] X.-Q. Sun, K. Farmer, and W. Carr, "A bistable microrelay based on two-segment multimorph cantilever actuators," in *Micro Electro Mechanical Systems, 1998. MEMS 98. Proceedings., The Eleventh Annual International Workshop on*, 1998, pp. 154-159.

[13] J. Qui, J. H. Lang, A. H. Slocum, and R. Strümpler, "A high-current electrothermal bistable MEMS relay," in *Micro Electro Mechanical Systems, 2003. MEMS-03 Kyoto. IEEE The Sixteenth Annual International Conference on*, 2003, pp. 64-67.

[14] B. Hälg, "On a nonvolatile memory cell based on micro-electro-mechanics," in *Micro Electro Mechanical Systems, 1990. Proceedings, An Investigation of Micro Structures, Sensors, Actuators, Machines and Robots. IEEE*, 1990, pp. 172-176.

[15] F. Mattioni, P. M. Weaver, K. D. Potter, and M. I. Friswell, "The application of thermally induced multistable composites to morphing aircraft structures," in *The 15th International Symposium on: Smart Structures and Materials & Nondestructive Evaluation and Health Monitoring*, 2008, pp. 693012-693012-11.

[16] C. G. Diaconu, P. M. Weaver, and F. Mattioni, "Concepts for morphing airfoil sections using bi-stable laminated composite structures," *Thin-Walled Structures,* vol. 46, pp. 689-701, 2008.

[17] A. F. Arrieta, O. Bilgen, M. I. Friswell, and P. Ermanni, "Modelling and configuration control of wing-shaped bi-stable piezoelectric composites under aerodynamic loads," *Aerospace Science and Technology,* vol. 29, pp. 453-461, 2013.

[18] N. Fichaux, J. Beurskens, P. H. Jensen, J. Wilkes, S. Frandsen, J. Sorensen, *et al.*, "Upwind: Design limits and solutions for very large wind turbines," *Sixth Framework Programme,* 2011.

[19] W. Hufenbach, M. Gude, and L. Kroll, "Design of multistable composites for application in adaptive structures," *Composites science and technology,* vol. 62, pp. 2201-2207, 2002.

[20] M. R. Schultz, M. W. Hyer, R. B. Williams, W. K. Wilkie, and D. J. Inman, "Snap-through of unsymmetric laminates using piezocomposite actuators," *Composites science and technology,* vol. 66, pp. 2442-2448, 2006.

[21] C. G. Diaconu, P. M. Weaver, and A. F. Arrieta, "Dynamic analysis of bi-stable composite plates," *Journal of Sound and Vibration,* vol. 322, pp. 987-1004, 2009.

[22] A. Arrieta, D. Wagg, and S. Neild, "Dynamic snap-through for morphing of bi-stable composite plates," *Journal of Intelligent Material Systems and Structures,* p. 1045389X10390248, 2010.

[23] A. Senba, T. Ikeda, and T. Ueda, "A two-way morphing actuation of bi-stable composites with piezoelectric fibers," *51ST AIAA/ASME/ASCE/AHS/ASC STRUCTURES, STRUCTURAL DYNAMICS, AND MATERIALS Conf. 2010: Orlando, Florida* 2010.

[24] U. Lindberg, J. Soderkvist, T. Lammerink, and M. Elwenspoek, "Quasi-buckling of micromachined beams," *Journal of Micromechanics and Microengineering,* vol. 3, p. 183, 1993.

[25] W. Fang and J. Wickert, "Post buckling of micromachined beams," *Journal of Micromechanics and Microengineering,* vol. 4, p. 116, 1994.

[26] M. Vangbo, "An analytical analysis of a compressed bistable buckled beam," *Sensors and Actuators A: Physical,* vol. 69, pp. 212-216, 1998.

[27] F. Moon and P. J. Holmes, "A magnetoelastic strange attractor," *Journal of Sound and Vibration,* vol. 65, pp. 275-296, 1979.

[28] M.-L. Dano and M. Hyer, "SMA-induced snap-through of unsymmetric fiber-reinforced composite laminates," *International Journal of Solids and Structures,* vol. 40, pp. 5949-5972, 2003.

[29] M. T. A. Saif, "On a tunable bistable MEMS-theory and experiment," *Microelectromechanical Systems, Journal of,* vol. 9, pp. 157-170, 2000.

[30] C. Maurini, J. Pouget, and S. Vidoli, "Distributed piezoelectric actuation of a bistable buckled beam," *European Journal of Mechanics-A/Solids,* vol. 26, pp. 837-853, 2007.

[31] W.-Y. Tseng and J. Dugundji, "Nonlinear vibrations of a buckled beam under harmonic excitation," *Journal of Applied Mechanics,* vol. 38, pp. 467-476, 1971.

[32] P. Holmes, "A nonlinear oscillator with a strange attractor," *Philosophical Transactions of the Royal Society of London. Series A, Mathematical and Physical Sciences,* vol. 292, pp. 419-448, 1979.

[33] D. Sun and L. Tong, "Static shape control of structures using nonlinear piezoelectric actuators with energy constraints," *Smart materials and structures,* vol. 13, p. 1059, 2004.

[34] C. Liang, F. Sun, and C. Rogers, "Coupled electro-mechanical analysis of adaptive material systems—determination of the actuator power consumption and system energy transfer," *Journal of Intelligent Material Systems and Structures,* vol. 5, pp. 12-20, 1994.

[35] M. C. Brennan and A.-M. R. McGowan, "Piezoelectric power requirements for active vibration control," in *Smart Structures and Materials' 97*, 1997, pp. 660-669.

[36] J. Sirohi and I. Chopra, "Actuator power reduction using LC oscillator circuits," *Journal of intelligent material systems and structures,* vol. 12, pp. 867-877, 2001.

[37] G. A. Lesieutre and C. L. Davis, "Can a coupling coefficient of a piezoelectric device be higher than those of its active material?," in *Smart Structures and Materials' 97*, 1997, pp. 281-292.

[38] A. F. Arrieta, O. Bilgen, M. I. Friswell, and P. Hagedorn, "Dynamic control for morphing of bi-stable composites," *Journal of Intelligent Material Systems and Structures,* vol. 24, pp. 266-273, 2013.

[39] R. Harne and K. Wang, "A review of the recent research on vibration energy harvesting via bistable systems," *Smart Materials and Structures,* vol. 22, p. 023001, 2013.

[40] S. P. Pellegrini, N. Tolou, M. Schenk, and J. L. Herder, "Bistable vibration energy harvesters: a review," *Journal of Intelligent Material Systems and Structures,* p. 1045389X12444940, 2012.

[41] G. Duffing, *Erzwungene Schwingungen bei veränderlicher Eigenfrequenz und ihre technische Bedeutung*: R, Vieweg & Sohn, 1918.

[42] A. H. Nayfeh and D. T. Mook, *Nonlinear oscillations*: John Wiley & Sons, 2008.

[43] A. H. Nayfeh, *Perturbation methods*: John Wiley & Sons, 2008.

[44] I. Kovacic and M. J. Brennan, *The Duffing equation: Nonlinear oscillators and their behaviour*: John Wiley & Sons, 2011.

[45] MathWorks. (March). *ode45*. Available: http://www.mathworks.com/help/matlab/ref/ode45.html

[46] M. Zarepoor and O. Bilgen, "Constrained-Energy Cross-Well Actuation of the Duffing-Holmes Oscillator," in *57th AIAA/ASCE/AHS/ASC Structures, Structural Dynamics, and Materials Conference*, 2016, p. 0201.

[47] M. Zarepoor and O. Bilgen, "Constrained-Energy Cross-Well Actuation of Bistable Structures," *AIAA Journal*, pp. 1-4, 2016.

[48] O. Bilgen, M. R. Simsek, and A. F. Arrieta, "Minimum Energy Cross-Well Actuation of Bistable Piezocomposite Unsymmetric Cross-Ply Plates," *ICAST2014: 25th International Conference on Adaptive Structures and Technologies* October 6-8 2014.

[49] O. Bilgen, M. I. Friswell, S. F. Ali, and G. Litak, "Broadband vibration energy harvesting from a vertical cantilever piezocomposite beam with tip mass," *International Journal of Structural Stability and Dynamics*, vol. 15, p. 1450038, 2015.

[50] R. Iyengar, "A nonlinear system under combined periodic and random excitation," *Journal of statistical physics*, vol. 44, pp. 907-920, 1986.

[51] V. Ingle and J. Proakis, *Digital signal processing using MATLAB*: Cengage Learning, 2011.

[52] G. Proakis John and G. Manolakis Dimitris, "Digital Signal Processing, principles, algorithms, and applications," *Pentice Hall*, 1996.

[53] MathWorks. (March). *firpm*. Available: http://www.mathworks.com/help/signal/ref/firpm.html

VITA

Masoud Zarepoor

Department of Mechanical and Aerospace Engineering
Old Dominion University
238 Kaufman Hall, Norfolk VA 23529

Email: mzare001@odu.edu
Voice: 757-663-3940

EDUCATION

M.Sc. in Mechanical Engineering (2013), Wright State University, Dayton, Ohio.
B.Sc. in Mechanical Engineering (2010), Shiraz University, Shiraz, Iran.

RESEARCH INTERESTS

- Nonlinear Vibrations
- Piezoelectric Materials
- Structural Dynamics
- Solid Mechanics
- Design and Fabrication

ACADEMIC EXPERIENCE

Graduate Teaching Assistant, Old Dominion University, August 2015-present
- Teaching Assistant for MAE 332, Mechanical Engineering Design I
- Teaching Assistant for MAE 220, Solid Mechanics

Graduate Research Assistant, Old Dominion University, August 2013-August 2015
Smart Systems Laboratory Manager, Old Dominion University, August 2013-August 2015
Graduate Research Assistant, THz Sensors group, Wright State University, April 2012-July 2013
Graduate Teaching Assistant, Wright State University, April 2012-June 2012
- Lab instructor for Mechanical Engineering lab

PUBLICATIONS

[3] M. Zarepoor and O. Bilgen, "Constrained-Energy Cross-Well Actuation of Bistable Structures," AIAA Journal, pp. 1-4, 2016, http://dx.doi.org/10.2514/1.J055148.

[2] M. Zarepoor and O. Bilgen, "Constrained-Energy Cross-Well Actuation of the Duffing-Holmes Oscillator", 57th AIAA/ASCE/AHS/ASC Structures, Structural Dynamics, and Materials Conference, AIAA SciTech, (AIAA 2016-0201).

[1] J. R. Middendorf, D. A. LeMaster, and M. Zarepoor, "*Design of Multi-Order Diffractive THz Lenses*", IRMMW-THz Symposium, Wollongong, Australia, September 23-28, 2012.